Spatiotemporal dynamics of DNA repair proteins between the Golgi and nucleus maintain genomic stability.

George Galea[1*]†, Karolina Kuodyte[1,2]†, Muzamil M. Khan[1,3], Peter Thul[4], Beate Neumann[5], Emma Lundberg[4,6,7], Rainer Pepperkok[1,3,5*]

[1] Cell Biology and Biophysics Unit, European Molecular Biology Laboratory (EMBL), 69117 Heidelberg, Germany
[2] Collaboration for joint PhD degree between EMBL and Heidelberg University, Faculty of Biosciences
[3] Translational Lung Research Center Heidelberg (TLRC), German Center for Lung Research (DZL), Heidelberg, Germany
[4] Science for Life Laboratory, School of Engineering Sciences in Chemistry, Biotechnology and Health, KTH - Royal Institute of Technology, Stockholm, 17121, Sweden.
[5] Advanced Light Microscopy Facility, EMBL, Heidelberg, 69117, Heidelberg, Germany
[6] Department of Bioengineering, Stanford University, Stanford, CA 94305, USA
[7] Department of Pathology, Stanford University, Stanford, CA 94305, USA

† These authors contributed equally.
* Corresponding authors: george.galea@embl.de; rainer.pepperkok@embl.org

Abstract

The Golgi complex is a key organelle of the secretory pathway, but also serves as a critical hub for maintaining cellular homeostasis, orchestrating various signalling pathways and essential cellular processes such as membrane trafficking and post-translational modifications. Despite its central role, the communication between the Golgi and the cell nucleus has remained largely unexplored. To bridge this gap, we have analysed and siRNA-validated localisation data of the Human Protein Atlas, finding an unexpected and significant level of interconnectivity between the proteomes of the Golgi complex and nucleus, including an intriguing involvement in DNA repair processes. Here, we uncovered a cluster of DNA repair proteins present in distinct sub-Golgi localisations as well as in the nuclear compartment. In response to genotoxic stress these proteins redistribute dynamically between the Golgi complex and the nucleus, with the specific type of DNA injury influencing this distribution pattern. To probe this Golgi–nucleus link, we examined the Homologous Recombination (HR) regulator RAD51C and find that DNA damage triggers ATM-dependent release of a Giantin-tethered Golgi pool and Importin-β–dependent nuclear import, where repair-associated nuclear foci form. Downregulation of Giantin prematurely releases RAD51C, producing RAD51C nuclear foci lacking key HR markers, reducing ATM activation, elevating genome instability, and accelerating cell proliferation. These findings support a timing-based pathway in which the Golgi acts as a spatiotemporal coordination node for HR regulators and other DDR factors. Our study sheds light on the dynamic interplay between the Golgi and the nucleus in safeguarding genomic stability while maintaining the delicate balance of cellular homeostasis.

Introduction

Eukaryotic cells have evolved a highly specialised and coordinated array of membrane-bounded organelles. This compartmentalisation allows the segregation of biochemical reactions, ensuring that they are carried out with the highest specificity and efficiency. However, organelles do not function in isolation but rely on the continual exchange of lipids, proteins and signalling cues to maintain cellular homeostasis. At the centre of this cross-coordination of subcellular transport and signalling pathways lies the Golgi complex. Thus, contributing well beyond its classical roles of membrane trafficking, and post-translational modification but also acting as a regulatory hub with numerous cellular processes intersecting at this organelle such as autophagy, mitosis, growth signalling, cytoskeletal and energy status regulation (Wilson et al. 2011; Makhoul, Gosavi, and Gleeson 2018). Perturbations to the Golgi architecture and mutations of its constituents have been associated with a wide array of human diseases such as neurodegenerative disorders and cancer, amongst many others (Freeze and Ng 2011; Machamer 2015; Zappa, Failli, and De Matteis 2018; Liu et al. 2021). Although we have a clearer picture of the Golgi's interactions and regulatory functions in the cytoplasmic domain, its communication with the nucleus remains largely unexplored.

Emerging themes have started to illustrate the relationship between the Golgi and nuclear compartment, with multi-localisation proteins playing a pivotal role. For example, in cholesterol homeostasis and endoplasmic reticulum (ER) stress response, sensing-signalling proteins SREBP and ATF6, respectively, get proteolytically cleaved at the Golgi complex to regulate gene expression through the release of a transcriptionally active amino

terminus that makes its way to the nucleus (Haze et al. 1999; Brown, Radhakrishnan, and Goldstein 2018). Few studies have also hinted at a link between cytoplasmic organelles, genomic stability, and, in turn, cancer, with the Golgi complex emerging as a central theme (Petrosyan 2015; Kulkarni-Gosavi, Makhoul, and Gleeson 2019; Zhang 2021). At a structural level, the Golgi undergoes dramatic morphological changes following the induction of DNA lesions, from ribbon-like perinuclear stack to dispersed fragments (Farber-Katz et al. 2014). A response requiring the phosphorylation of the Golgi resident oncoprotein, Golgi phosphoprotein 3 (GOLPH3), by DNA-dependent protein kinase (DNA-PK), a DNA Damage Response (DDR) regulator (Farber-Katz et al. 2014). Golgi morphology alterations are also a common feature across a wide variety of cancer types and are often reflected in changes in the distribution of Golgi resident proteins (Petrosyan 2015; Zhang 2021). Rearrangement of Golgi glycosyltransferases distribution is a recurrent phenomenon in cancer cells, resulting in defective glycosylation, a process thought to promote cancer development (Petrosyan 2015; Zhang 2021; Bui et al. 2021). These studies hint at a clear link between Golgi and nucleus as communicating organelles, however a systematic approach that could pin down the signalling pathways involved in this communication has been missing.

To this end, here, we utilise a localisation data and antibody resources from the Human Protein Atlas (HPA) project (Thul et al. 2017) to explore a class of multi-localisation proteins as a systematic strategy to identify key signalling pathways that function between the Golgi and nuclear compartment. We validate candidate Golgi–nuclear localisations by siRNA-mediated knockdown revealing a network of DNA repair proteins localised at the Golgi complex. We systematically analyse their subcellular localisation within the Golgi, as well as their redistribution patterns in response to different types of DNA damage. Building on these observations, we propose a spatiotemporal regulatory pathway for DDR control between the Golgi complex and nucleus that gates the timed availability of HR regulators. Using RAD51C as a representative HR factor, we find that a Golgi resident pool is released to the nucleus upon DNA damage where it forms repair associated foci, and that the Golgi scaffold Giantin (GOLGB1) is required for RAD51C localisation to the Golgi. Disrupting this regulation through Giantin depletion leads to premature nuclear accumulation of RAD51C, modulation of upstream ATM signalling, increased genomic instability, and accelerated cell proliferation. Together, these findings highlight the importance of spatial regulation of DDR proteins in maintaining genomic integrity and cellular homeostasis, and suggest a broader role for the Golgi as a regulatory platform in DNA repair.

Results

Antibody-based systematic analysis and siRNA-mediated validation identifies a network of DNA damage response proteins at the Golgi complex.

To systematically explore candidates that might link Golgi to nuclear function or vice versa, we shortlisted 329 proteins annotated by the Human Protein Atlas (HPA) project (Thul et al. 2017) to localise at both Golgi-like membranes and the nucleus **(Figure 1A)**. To ensure the specificity of both localisation data and antibody binding, we tested the corresponding HPA antibody for each candidate using an siRNA-mediated knockdown pipeline (Stadler et al. 2012). This approach was specifically designed to exclude false localisation arising from antibody cross-reactivity. A reduction of at least 25% in both nuclear and Golgi signals following knockdown was required for validation.

Using this strategy, we confirmed the dual localisation for 163 proteins (167 HPA antibodies) **(Figure 1B and Table S1)**. Bioinformatic analysis of the identified 163 candidates revealed a number of functional protein networks **(Figure 1B)**, primarily composed of two major pathways: membrane trafficking and surprisingly, DNA Damage Response (DDR) **(Figures 1B and 1C)**. Additionally, we identified enrichment for cell cycle regulation, RNA metabolism, and lipid metabolism regulators **(Table S1 and Figure S2B)**. Within the membrane trafficking enriched cluster, we identified several essential components of intra-Golgi trafficking machinery, including Golgins, SNAREs, COG tethering complex, and RAB GTPase exchange factors **(Figure 1B)**.

An enriched cluster centred on the DDR emerged through the combination of DNA repair proteins and an array of cell cycle regulators (**Figures 1D, S1, S2A and S2B**). Within this cluster, we identified various proteins collectively spanning the core DNA repair pathways (Homologous Recombination (HR); Mismatch Repair (MMR); Microhomology-Mediated End Joining (MMEJ) and Base Excision Repair (BER)) as well as other integral regulators of DDR such as ubiquitination, cell cycle and signalling **(Figures 1D and 1E)**. These surprising findings of DNA repair proteins at the Golgi prompted us to explore the links between DDR and Golgi function.

Golgi cisternal localisation analysis of dual-localising DDR proteins identifies specific distribution patterns that correlate with their function.

To start addressing the meaning of DDR proteins localisation at the Golgi complex and further validate their localisation, we shortlisted 15 candidates based on their described role in this pathway and conducted an analysis of their subcellular distribution within the organelle. The Golgi apparatus consists of *cis*-, *medial*, and *trans*-Golgi cisternae, extending into a tubular *trans*-Golgi network (TGN), with resident proteins strategically distributed along the Golgi stack in order to serve their function (Kulkarni-Gosavi, Makhoul, and Gleeson 2019). Since the ribbon-like Golgi structures make subdomain mapping difficult, we used nocodazole treatment to disperse the ribbon into isolated mini-stacks, a standard approach that enables high-resolution analysis of cisternal distribution (Dejgaard et al. 2007). We then performed confocal microscopy with co-staining for the *cis*-Golgi marker GM130 and the *trans*-Golgi marker TGN46. Fluorescence intensity line profiles were acquired across individual mini-stacks, and the relative localisation of each DDR protein was quantified by calculating Pearson's correlation coefficients (PCC) with the *cis*- and *trans*-markers (Dejgaard et al. 2007) **(Figures 2A–2E**, **S3D and Table S2**).

This analysis resolved three major localisation patterns throughout the Golgi cisternae: (i) a subset preferentially correlating with the *trans*-Golgi marker, TGN46 **(Figures 2A, 2B and 2E**), (ii) proteins correlating with the *cis*-Golgi marker, GM130 **(Figures 2C, 2D and 2E**); and (iii) proteins without a strong preference for either marker. Although the number of proteins examined was limited, emerging trends suggest pathway-related distribution (**Figure 2E**). For instance, BER and MMEJ proteins TOPORS, LIG1, and POLQ exhibited co-localisation with the *trans*-Golgi marker, TGN46, while HR factors NBN (Nibrin) and RAD51C have a high correlation with the *cis*-Golgi marker, GM130.

191 These observations suggested that DDR proteins may not only localise to the Golgi but also
192 occupy distinct cisternal subdomains, raising the possibility that sub-Golgi positioning could
193 influence how different repair pathways respond to DNA damage. We therefore next
194 examined whether these proteins dynamically redistribute between the Golgi and the nucleus
195 in response to genotoxic stress.
196
197 **Dual-localising DDR proteins dynamically redistribute between the Golgi and nucleus**
198 **in response to specific types of DNA injuries.**
199
200 We next examined whether DDR proteins with dual Golgi-nuclear localisation respond
201 dynamically to DNA damage. To this end, we compared two classes of DNA damage: double-
202 strand DNA breaks (DSBs) induced by doxorubicin (DOX), which intercalates into DNA
203 (Thorn et al. 2011) and oxidative DNA lesions induced by hydrogen peroxide (H_2O_2) (Henle
204 and Linn 1997) or potassium bromate ($KBrO_3$) (Loft et al. 1998) **(Figures 2F–2H and S3–**
205 **S5**).
206
207 Using this experimental approach we monitored for any genotoxic stress-induced changes
208 in protein distribution pattern of the 15 Golgi-nuclear localising DDR proteins. Initial
209 inspection revealed that all three treatments triggered marked changes in both the subcellular
210 localisation distribution and the overall signal intensity of many of the 15 proteins tested. Two
211 predominant redistribution patterns were observed: either in a Golgi-to-nuclear manner or
212 conversely, in a nucleus-to-Golgi direction. To quantify these shifts, we measured
213 fluorescence intensities in Golgi and nuclear masks and calculated a Golgi-to-nuclear
214 distribution ratio for each protein. Ratios <1 indicate Golgi-to-nuclear redistribution, whereas
215 ratios >1 reflect nucleus-to-Golgi shifts. This approach normalised for differences in protein
216 abundance and cell-to-cell heterogeneity.
217
218 The quantifications of the Golgi-nuclear ratio revealed a correlation between the redistribution
219 patterns of these DDR proteins and their subcellular distribution with the Golgi complex.
220 Here, treatment with DOX **(Figures 2F, 2G and S3**) resulted in a predominantly uniform
221 localisation pattern change, where *cis*-Golgi DDR proteins (3 out of 4) shifted from the Golgi
222 to the nucleus, whereas *trans*-Golgi proteins (7 out of 8) displayed a redistribution pattern
223 from the nucleus to the Golgi. Conversely, exposure to H_2O_2 or $KBrO_3$ **(Figures 2F, 2H, S4**
224 **and S5**) elicited the opposite response, with the majority of *trans*-Golgi DDR proteins (7 out
225 of 8) displaying a redistribution from the nuclear compartment to the Golgi while 2 out of the
226 4 *cis*-Golgi DDR proteins displayed a redistribution pattern from the nucleus to the Golgi.
227
228 When analysed by pathway annotation, broad distinctions also emerge, BER proteins
229 (TOPORS and LIG1) and MMEJ factor POLQ shifted from nucleus to Golgi in response to
230 DOX, whereas the MMR protein MSH6 and HR-associated proteins (RAD51C and NBN)
231 redistributed from Golgi to nucleus **(Figures 2G and S3)**. Specifically, with DOX treatment,
232 BER and MMEJ proteins shifted from the nucleus to the Golgi, while MMR and HR proteins
233 relocated from the Golgi to the nucleus. Conversely, this trend was reversed with H_2O_2 or
234 $KBrO_3$ treatments **(Figures 2H, S4 and S5)**.
235
236 While pathway-level trends were evident, some proteins (for example CCAR1) exhibited
237 similar directionality under DOX and H_2O_2, underscoring that pathway membership is not
238 exclusive and many DDR factors act in multiple contexts. Several proteins participate in

multiple repair contexts, complicating binary distinction between different pathways. Nonetheless, these findings demonstrate that DDR proteins redistribute between Golgi and nucleus in a manner that depends on both the type of DNA lesion and their steady-state Golgi cisternal localisation.

Redistribution of RAD51C Golgi fraction is required for the formation of RAD51C repair nuclear foci and is dependent on the kinase ATM.

To mechanistically dissect the novel link between the Golgi complex and the nucleus, we characterised the Homologous Recombination (HR) repair protein RAD51C. As a member of the RAD51 paralog family, RAD51C is essential for regulating HR-mediated repair of double-strand breaks (DSBs). Previous studies have demonstrated RAD51C's involvement across multiple stages of HR repair: promoting the DNA damage checkpoint (Badie et al. 2009), aiding in RAD51 filament formation, stabilising replication forks, and resolving Holliday junctions to complete repair (Prakash et al. 2022; Rawal et al. 2023; Greenhough et al. 2023). RAD51C also functions in replication stress responses (Somyajit, Subramanya, and Nagaraju 2012) underscoring its versatility. This multifunctionality, combined with a substantial Golgi-localised population compared to other DDR proteins in our screen, prompted us to investigate RAD51C as a representative candidate for understanding how Golgi-associated DDR factors are dynamically recruited to repair complexes. Notably, RAD51C contains both a nuclear localisation signal (NLS) and a nuclear export signal (NES) (Miller et al. 2005), which may enable it to shuttle between the Golgi and the nucleus in response to DNA damage, thereby supporting its role in replication fork stabilisation and HR repair.

Following the identification of RAD51C as a dual-localising DDR protein in our initial HPA-based antibody screen, we sought to further validate its localisation using two additional commercial antibodies targeting distinct RAD51C epitopes. In total, three distinct antibodies were used: the original HPA antibody from the primary screen, a second antibody for independent immunofluorescence validation, and a third antibody for biochemical fractionation. Our immunofluorescence across across several cell lines confirmed RAD51C enrichment in a juxtanuclear compartment co-localising with the Golgi marker GM130 (**indicated by the yellow arrowhead; Figures 3A and 3B**), together with diffused cytoplasmic staining and discrete nuclear foci (**indicated by white arrowheads; Figures 3A and 3B)**. The specificity of the antibodies was confirmed by the depletion of RAD51C in HeLa Kyoto (HeLa-K) cells (**Figures S6A–S6C**). To corroborate these results biochemically, we fractionated HeLa-K cell lysates into nuclear, membrane and cytoplasmic compartments. RAD51C was detected in all fractions, with the majority present in the membrane and cytoplasmic pool (**Figures 3C and 3D**) consistent with the immunofluorescence data.

Although RAD51C has been extensively characterised biochemically and structurally, previous studies have examined its subcellular distribution. Earlier work has largely focused on *in vitro* complex formation and DNA repair mechanisms, rather than on the spatial distribution, likely contributing to the Golgi-associated pool remaining unrecognised. Although previous work, notably *Badie et al.* (2009), has shown a juxtanuclear RAD51C signal (see Fig. 1D of that study), this localisation was not further discussed.

286 Having established the steady-state RAD51C Golgi localisation, we next examined RAD51C
287 dynamics following DSB induction with doxorubicin (DOX). Upon drug addition (**Figures 3E-**
288 **3H**), we observed an overall decrease in RAD51C protein level, with the Golgi-localised
289 fraction (co-localised with GM130, **yellow arrows**) decreasing more rapidly than the nuclear
290 fraction. Concurrently, the diffused nuclear RAD51C pattern changed into very distinct
291 nuclear foci (**white arrows**), which become more pronounced with longer DOX exposure
292 (**Figure 3E**).
293
294 Quantitative analysis of these experiments allowed us to measure the changes in RAD51C
295 levels at both the Golgi (**Figure 3F**) and the nuclear compartment (**Figure 3G**), and to
296 calculate a RAD51C Golgi-nuclear distribution ratio (**Figure 3H**). This redistribution was
297 further validated by subcellular fractionation (**Figures 3I and S6D**). Similarly, the total protein
298 level of RAD51C is observed to decrease after 3 h treatment, with a much larger reduction
299 in the membrane compartment when compared to the nuclear fraction. Additionally, we
300 observed an increase in RAD51C cytoplasmic fraction with DOX treatment. Overall, in both
301 experiments, the RAD51C Golgi-nucleus distribution ratio is seen to decrease significantly
302 after 3 h DOX treatment in both the immunofluorescence and biochemical assay (**Figures**
303 **3H and 3I).**
304
305 To identify a mechanism for RAD51C redistribution between compartments, we induced
306 DSBs using DOX while inhibiting Importin-β-mediated nuclear import with the small peptide
307 inhibitor Importazole (IPZ) (Soderholm et al. 2011). IPZ treatment (**Figures 3J–3L and S7A;**
308 **Golgi fraction marked with yellow arrows; nuclear foci marker with white arrows**)
309 inhibited the DOX-induced RAD51C redistribution. Instead, the majority of the protein
310 population remained co-localised with the Golgi marker, GM130, and nuclear foci formation
311 was significantly inhibited **(Figure 3J)**. While a reduction in the overall RAD51C protein level
312 was measured with DOX treatment alone, no significant change in the RAD51C distribution
313 pattern was observed with IPZ treatment (**Figure S7A)**. Unexpectedly, although DOX alone
314 triggers dissociation of the Golgi RAD51C pool, under DOX plus IPZ RAD51C remained
315 Golgi localised, suggesting that Importin-β dependent transport may contribute to or be tightly
316 coupled with the RAD51C dissociation step.
317
318 We next sought to test whether the phosphorylation of DDR kinases mediate RAD51C
319 redistribution in response to DSBs. The three master kinases that are active in response to
320 DNA damage are ataxia telangiectasia mutated (ATM), ataxia telangiectasia and Rad3-
321 related (ATR) and DNA-dependent protein kinase (DNA-PK) (Ciccia and Elledge 2010). Cells
322 were treated with phosphorylation inhibitors specific for each kinase and RAD51C
323 redistribution was analysed following DOX treatment (**Figures 3M–3O and S7B; Golgi**
324 **fraction marked with yellow arrows**). DOX combined with the ATM phosphorylation
325 inhibitor, KU55933 (Hickson et al. 2004) significantly inhibited RAD51C redistribution, with
326 the majority of the protein remaining co-localised with GM130 and nuclear foci formation
327 blocked **(Figure 3M)**. In contrast, the combined treatment of DOX with ATR or DNA-PK
328 phosphorylation inhibitors, VE-821 (Fokas et al. 2012) and NU7441 (Tavecchio et al. 2012)
329 respectively, had no apparent impact on the redistribution of RAD51C when compared with
330 cells treated with DOX only**.** Inhibitor-only treatments did not alter RAD51C localisation
331 (**Figure S7B**).
332

333 To confirm that these observations were a direct result of DSBs and not an off-target drug
334 effect, we tested other DSB-causing agents (Jekimovs et al. 2014): camptothecin (CPT)
335 (**Figures S8A–S8C**), etoposide (ETO) (**Figures S8D–S8F**), and mitomycin C (MMC)
336 (**Figures S8G–S8I**). All treatments led to significant RAD51C redistribution from the Golgi to
337 the nuclear compartment. Notably, CPT treatment (**Figure S8A**) caused a shift in nuclear
338 RAD51C from a **diffuse distribution to distinct foci**, while ETO or MMC treatments
339 (**Figures S8D and S8G**) increased the nuclear RAD51C population without obvious foci
340 formation. These distinct nuclear phenotypes likely reflect lesion class and timing: CPT
341 generates replication associated breaks that favour discrete HR foci, whereas ETO (Topo II
342 poisoning) and MMC (interstrand crosslinks) produce damage that, within our treatment
343 window, increases nuclear RAD51C without prominent puncta.
344
345 **Golgi localisation of RAD51C is dependent on the Golgin Giantin.**
346
347 To identify potential Golgi membrane anchors for RAD51C, we re-analysed two
348 independent, previously published genome-wide siRNA datasets that profiled HR and DDR
349 regulators (Paulsen 2010; Adamson et al. 2012). Interestingly these screens contained
350 multiple Golgin protein family members as hit candidate genes, in particular the knockdown
351 of Giantin and GMAP210 led to a significant reduction in HR repair rates (Adamson et al.
352 2012) (**Golgin results summarised in Figure S9A**), and the depletion of Giantin
353 significantly inhibited H2AX phosphorylation, a crucial event in DDR signalling regulation
354 (Paulsen 2010) (**Golgin results summarised Figure S9B**). Given the structural properties
355 of Golgins (**Figure 4A**), which are predominantly coiled-coil proteins anchored to the Golgi
356 membrane by their carboxy terminus and projected into the surrounding cytoplasm (Witkos
357 and Lowe 2015), they are ideally suited for capturing or tethering nearby membranes and
358 potentially retaining DDR proteins such as RAD51C.
359
360 To investigate whether RAD51C localisation is dependent on these Golgins, we performed
361 siRNA-mediated depletion of Giantin and GMAP210, and compared their effects on RAD51C
362 distribution to a control siRNA treatment (**Figures 4B–4E**). GMAP210 depletion had no
363 significant effect on RAD51C distribution, whereas Giantin knockdown led to a notable
364 redistribution of RAD51C (**Figure 4B**). Specifically, we observed a marked decrease in
365 RAD51C co-localisation with the Golgi marker GM130 (**yellow arrows**) and an increase in
366 nuclear RAD51C localisation with distinct bright nuclear foci appearing (**white arrows**)
367 (**Figure 4B**). Quantifications revealed a significant reduction of the RAD51C Golgi
368 population, (**Figure 4C**) and the distribution ratio (**Figure 4D**) reduced by more than half. The
369 number of RAD51C foci (**Figure 4E**) increased by more than two-fold upon depletion of
370 Giantin with either siRNAs. There was no significant difference in either RAD51C Golgi
371 intensity, distribution ratio or foci number (**Figures 4C–4E**) between the GMAP210-depleted
372 and control cells. The effective knockdown of Giantin (**Figure S9C**) and GMAP210 was
373 tested by immunofluorescence. Sub-Golgi cisternae localisation analysis confirmed that
374 Giantin and RAD51C are distributed in a similar manner throughout the organelle (**Figure 4F**
375 **and G**).
376
377 To determine if RAD51C physically interacts or is part of a larger complex with Giantin we
378 performed an immunoprecipitation (IP) assay (**Figures 4H and 4I**). Endogenous Giantin and
379 RAD51C were found to co-IP from HeLa-K protein extracts (**Figure 4H**). To explore the
380 dynamics of this interaction in response to DNA damage, we induced DSBs and performed

co-IP experiments (**Figure 4I**). Our results showed that RAD51C and Giantin dissociate upon DSB induction. However, co-treatment with either an ATM inhibitor or IPZ, alongside doxorubicin, prevented this dissociation, corroborating our earlier immunofluorescence observations (**Figures 3E–3O**).

To gain insight into the nature of RAD51C foci induced by Giantin depletion, we carried out co-localisation assays to determine whether these structures contain standard HR markers, phosphorylated H2AX (γ-H2AX) (**Figures 4J and 4K**) and phosphorylated ATM (p-ATM) (**Figures 4L and 4M**) under physiological conditions and induction of DSBs by ETO. Both proteins are well-established markers for DSB repair sites and are important for the recruitment of the HR repair machinery (Vítor et al. 2020). In cells treated with a control siRNA, we observed that approximately half of the RAD51C nuclear foci were decorated with either γ-H2AX or p-ATM (**Figures 4J–4M**; **colocalising foci are denoted with an arrow**), as previously described (Vítor et al. 2020). RAD51C foci induced by the depletion of Giantin, however, showed significantly lower co-localisation with both markers regardless of DSBs induction. Overall, Giantin-depleted cells showed fewer γ-H2AX and p-ATM nuclear foci, consistent with previous reports (Paulsen 2010) (**Figure S9B**).

Giantin depletion increases genomic instability and cell proliferation while inhibiting ATM signalling.

Having built evidence that Giantin regulates Golgi tethering of RAD51C and its DNA damage–triggered release, we asked whether downregulation of Giantin impacts genome stability and DDR signalling. We analysed GMAP210 alongside Giantin because prior HR/DDRs screens implicated both Golgins (Paulsen 2010; Adamson et al. 2012). As a first readout, we assessed micronuclei formation, a well-established marker of genotoxic stress (**Figures 5A–5C**) (Krupina, Goginashvili, and Cleveland 2021). Under basal conditions, depletion of Giantin or RAD51C significantly increased the percentage of cells displaying micronuclei and aberrant nuclear structures compared to controls, while GMAP210 knockdown had no significant effect (**Figure 5B**). To test repair capacity, we induced DNA damage and allowed recovery (**Figure 5C**). Strikingly, after recovery both GMAP210 and Giantin knockdown led to a sustained and significant increase in micronuclei formation post-recovery, indicating persistent genomic instability and defective repair dynamics. Because our mechanistic model centres on a Giantin–RAD51C tether and the strongest basal phenotype mapped to Giantin, subsequent assays focus on Giantin.

To corroborate basal genomic instability, we performed comet assays (Møller 2018) to measure levels of fragmented genomic DNA (**Figures 5D and 5E**). Cells with defective DNA repair or exposed to DNA-damaging agents display long comet tails, whereas healthy cells show shorter or no tails. Knockdown of Giantin or RAD51C resulted in notably longer comet tails compared to control siRNA treatment (**Figure 5D**). Quantification revealed a 2.5-fold increase in tail length and fluorescence intensity for RAD51C-depleted cells, and 1.8 to 1.6-fold increases for Giantin-depleted cells (siGiantin#1 and siGiantin#2, respectively) (**Figure 5E**).

We next examined the long-term consequences on cell proliferation and colony formation in HeLa-K and U-2 OS cells (**Figures 5F–5I**). Giantin knockdown significantly enhanced both proliferation and colony formation. To determine whether these effects were associated with

429 cell cycle changes, we analysed the cell cycle profiles of Giantin-depleted cells via FACS
430 (**Figure S9D**). No significant cell cycle alterations were detected, suggesting that the
431 increased proliferation is not due to major cell cycle perturbations.
432
433 Having observed that Giantin knockdown increases basal genomic instability and displaces
434 RAD51C from the Golgi, we next assessed ATM activation as a proximal readout of HR-
435 linked DDR signalling. To explore this, we assessed the ability of cells depleted of Giantin to
436 initiate HR by measuring ATM phosphorylation, the master regulator of this pathway (**Figures**
437 **5J**). In control siRNA treated cells, DOX treatment increased phosphorylated ATM levels in
438 response to DSBs. However, Giantin-depleted cells (**Figure 5J**) showed significantly lower
439 ATM phosphorylation levels under the same conditions.To investigate whether the
440 redistribution of HR factors from the Golgi to the nucleus plays a role in ATM signalling, we
441 used Importazole (IPZ) to inhibit Importin-β-mediated nuclear import and subsequently
442 induced DSBs with DOX (**Figure 5K**). Here, we found that IPZ treatment did not significantly
443 alter ATM signalling, regardless of the induction of DSBs. These findings suggest that the
444 regulated redistribution of HR factors is less impactful on ATM signalling than their
445 mislocalisation, implying that Giantin's spatial regulation of HR factors is crucial for proper
446 ATM activation.
447
448 We next asked whether perturbing RAD51C could modulate the signalling and stability
449 phenotypes observed with Giantin loss. To this end, we carried out co-depletion of RAD51C
450 and Giantin, along with single depletions (**Figures 5L and 5M**). Consistent with previous
451 observations, Giantin knockdown led to a significant decrease in ATM phosphorylation levels,
452 while RAD51C knockdown increased ATM phosphorylation. Co-depletion of RAD51C and
453 Giantin restored ATM phosphorylation levels to those comparable to control cells. To validate
454 the restoration of DDR signalling through co-depletion, we assessed genomic stability via
455 micronuclei incidence (**Figure 5N**). Individual knockdowns of Giantin and RAD51C elevated
456 micronuclei formation, indicative of genomic instability, whereas co-depletion significantly
457 reduced micronuclei incidence, approaching levels observed in control cells. Lastly, we
458 evaluated cell proliferation (**Figure 5O**). While Giantin knockdown enhanced cell proliferation
459 and RAD51C knockdown diminished it, co-depletion resulted in proliferation rates
460 comparable to control. These results are consistent with RAD51C contributing to the Giantin
461 dependent timing mechanism, while not excluding roles for additional Golgi associated
462 factors.
463
464 **Discussion**
465
466 In this study, we reveal evidence for a previously underappreciated and functionally
467 meaningful spatiotemporal regulatory system connecting the Golgi complex and the nucleus,
468 with broad potential implications for homologous recombination (HR) and other DNA repair
469 pathways. Our analysis of Human Protein Atlas (HPA) localisation data (Thul et al. 2017) and
470 experimental validation via siRNA knockdowns uncovered numerous double-localising Golgi-
471 nuclear proteins. Among these, we identified a cluster of DNA repair proteins that exhibit
472 steady-state localisation in both compartments. This cluster encompasses crucial regulatory
473 proteins involved in various DNA repair pathways (**Figure 1D**), not only specific for HR-
474 mediated DNA repair but also Mismatch Repair (MMR), Base Excision DNA Repair (BER)
475 and Microhomology-Mediated End Joining (MMEJ), as well as other integral regulators of
476 DNA repair cellular responses such as chromatin cohesion, ubiquitination, cell cycle

477 regulation and signalling. Taken together, these observations support the existence of a DNA
478 repair protein network that localises to both the Golgi complex and the nucleus, positioning
479 the Golgi as a coordination node that links cytoplasmic organisation with nuclear repair
480 programmes.
481
482 Our systematic analysis revealed enrichment of subsets of these DNA repair proteins in
483 distinct sub-Golgi regions. This suggests a compartmentalised platform where components
484 of related DNA repair pathways gather, which could facilitate protein–protein interactions and
485 tune the timing and specificity of downstream signaling. The enriched association of the Golgi
486 scaffold Giantin with HR factors suggests a structural or scaffolding role in organising these
487 repair proteins. These Golgi-resident proteins may stabilise DDR factors at the Golgi and
488 help regulate their release to the nucleus. The close association between Golgins and DNA
489 repair kinases, such as ATM, supports the notion that the Golgi may provide a spatial context
490 for phosphorylation and assembly events. Such spatial organisation could help preserve
491 pathway fidelity by discouraging premature activation and by supporting timely recruitment
492 of DNA damage response components.
493
494 In response to genotoxic stress, we observed dynamic shuttling of DNA repair factors
495 between the Golgi and the nucleus, dependent on the type of DNA damage. The correlation
496 between steady-state Golgi localisation and their redistribution patterns upon DNA damage
497 is consistent with a role for the Golgi in temporally coordinating DDR. We propose that the
498 Golgi clusters DDR proteins during steady-state conditions and releases them to the nucleus
499 when damage is detected. In this model, spatiotemporal partitioning functions as a potential
500 checkpoint that coordinates repair factor dosage and timing, thereby integrating cytoplasmic
501 signals with nuclear lesions. Analogous behaviour has been described for shuttling proteins
502 such as BRCA1, whose movements between nucleus and cytoplasm modulate DNA repair,
503 cell cycle regulation and apoptosis (Rodriguez et al. 2004; Feng et al. 2004; Thompson
504 2010). By extension, Golgi mediated spatiotemporal control of multiple factors may contribute
505 to maintaining genomic stability.
506
507 To explore this spatiotemporal regulation, we outline a pathway linking the Golgi to HR repair
508 **(Figure 5P)**. Based on our findings and consistent with established models, we propose that
509 the pathway begins with the detection of double-strand DNA breaks (DSBs) in the nucleus
510 by the MRN complex, which activates ATM kinase. Although canonical MRN function is
511 indispensable for initiating ATM activation at DNA breaks, our data indicate that once ATM
512 is activated in the nucleus, an ATM-dependent signal or possibly a fraction of active ATM
513 can subsequently access the Golgi (Ovejero et al. 2023). In this view, the Golgi acts
514 downstream of the break sensor as an amplification and timing module rather than a primary
515 sensor, representing an organelle level checkpoint that conditions release on damage
516 context, akin to cytoplasmic ATM pools observed in oxidative stress responses (Shiloh and
517 Ziv 2013). Consistent with this model, Golgi-associated scaffolding and kinase activities
518 would be expected to gate the timed availability of a subset of HR regulators for lesion
519 engagement.
520
521 Within this framework, our data places Giantin as a spatial modulator of this Golgi-nuclear
522 timing system. Giantin depletion increases basal genomic instability, accelerates cell
523 proliferation, reduces ATM activation after DSB induction while displacing a RAD51C pool to
524 the nucleus. RAD51C depletion alone elevates genome instability but increases

525 phosphorylated ATM after damage, while co-depletion of RAD51C with Giantin partially
526 restores phosphorylated ATM and genome stability toward control and attenuates the Giantin
527 dependent proliferation increase. These findings are consistent with Giantin acting through
528 RAD51C as one conduit, while likely engaging other additional Golgi localising DNA damage
529 response factors.
530
531 RAD51C's known function can plausibly account for part of the Giantin loss phenotype. As a
532 member of the RAD51 paralog complexes BCDX2 and CX3, RAD51C executes essential
533 roles in stabilising replication forks, promoting RAD51 filament assembly, and resolving
534 Holliday junctions (Rein, Bernstein, and Baldock 2021; Sullivan and Bernstein 2018). In
535 principle, mislocalisation could undermine these processes, for example by altering the
536 recruitment of repair factors and DDR signalling with downstream effects on other factors
537 such as CHK2 (Badie et al. 2009; Somyajit, Subramanya, and Nagaraju 2012). As a central
538 participant in HR, RAD51C orchestrates RAD51 filament formation and subsequent strand
539 invasion steps required for DSB repair (Somyajit et al. 2015; Prakash et al. 2022). If
540 prematurely released to the nucleus or improperly retained at the Golgi, RAD51 filaments
541 may be disorganised or suboptimally assembled, leading to error-prone repair events.
542 RAD51C also influences checkpoint signaling by stabilising replication forks and interacting
543 with ATR–RPA, enabling proper CHK2 phosphorylation and cell-cycle arrest upon DNA
544 damage (Badie et al. 2009; Berti et al. 2020). Dysregulation of these checkpoint pathways
545 could encourage cells to progress through the cell cycle despite harboring DNA lesions and
546 alter DDR signalling.
547
548 Beyond RAD51C, our screen identified other DDR regulators with dual Golgi–nuclear
549 localisation, notably the HR regulator NBN, and candidates spanning chromatin regulation,
550 ubiquitination and checkpoint signalling. These observations argue for a cohort model in
551 which multiple Golgi-proximal factors are clustered at steady state and released with tuned
552 timing, such that their combined availability, rather than any single protein alone shapes HR
553 pathway behaviour and replication-stress responses. In this view, the Golgi provides a
554 spatiotemporal checkpoint that modulates factor dosage and order of arrival at lesions. Our
555 dataset supports this timing perspective through changes in upstream signalling and
556 genome-stability metrics, but does not dissect how HR repair efficiency is impacted; any
557 effect on HR therefore remains a testable prediction. Systematic follow-up should broaden
558 the catalogue of Golgi-associated DDR factors, benchmark their relative contributions, and
559 couple temporal proteomics with multiplex perturbations to resolve how joint release kinetics
560 influence HR fidelity and fork protection and restart.
561
562 In a clinical context, perturbation of Golgins, including Giantin, has been linked to elevated
563 breast cancer risk (Wang et al. 2020; Craven, Gökmen-Polar, and Badve 2021; Mathioudaki
564 et al. 2021; Pipek et al. 2023; Ghannoum et al. 2023; Leighton et al. 2023), as well as
565 decreased patient survival (**Figures S9E and S9F**) (Győrffy 2021; Ősz, Lánczky, and Győrffy
566 2021). Together with reports implicating additional Golgin family members across various
567 cancers (Baschieri et al. 2015; Bhat et al. 2017), these associates are compatible with a
568 broader role for Golgi scaffolding and signaling processes in controlling genomic integrity.
569 This raises the prospect of therapeutically modulating organelle-level checkpoints either by
570 tuning Golgi-dependent timing of factor release or by leveraging Golgi–nuclear
571 communication to sensitise tumours to genotoxic agents.
572

573 Finally, the observation that many other proteins dually localise to the Golgi and nucleus,
574 spanning membrane trafficking, RNA metabolism, and lipid regulation, supports the concept
575 of the Golgi as a dynamic integration hub for multiple essential pathways. Its proposed role
576 in DNA repair orchestration may extend beyond HR to additional DDR networks. Altogether,
577 these findings motivate a shift from purely concentration-based models of the DDR to timing-
578 aware, compartment-resolved models, opening new avenues for both fundamental research
579 and translational approaches in DNA repair and cancer biology.
580
581 **Figure legends**
582
583 **Figure 1: Antibody-based analysis identifies a network of DNA damage response**
584 **(DDR) proteins at the Golgi complex**
585 (**A**) Schematic diagram of the screening process for the shortlisting, validation and
586 characterisation of Golgi-nuclear localisation proteins, as a strategy to identify linking
587 pathways.
588 (**B**) Experimentally-based protein-protein interaction network displaying the DNA repair and
589 membrane trafficking Golgi-nuclear localisation proteins validated in this study; categorised
590 by functional pathways.
591 (**C**) Pathway enrichment analysis of the Golgi-nuclear localisation proteins identified in this
592 study.
593 (**D**) Experimentally-based STRING protein-protein interaction network showing the DDR
594 proteins identified to localise to both the Golgi complex and nucleus; yellow nodes indicate
595 double-localising proteins, and grey nodes are filler untested proteins.
596 (**E**) Representative images of HeLa-K cells stained with Human Protein Atlas (HPA)
597 antibodies against Golgi-nuclear DDR proteins (green), and the Golgi marker GM130 (red).
598 DNA was stained with Hoechst 33342 (blue). Yellow arrowheads denote the Golgi complex.
599 Scale bar, 10 μm.
600
601 **Figure 2: Systematic analysis of Golgi-nuclear DDR proteins localisation**
602 (**A–E**) Golgi-cisternal localisation analysis of Golgi-nuclear DDR proteins. HeLa-K cells were
603 treated with nocodazole (33 μM, 3 h), fixed and stained with antibodies against DDR proteins.
604 (**A–C**) Enlarged view of single isolated mini-stack, where cells were stained with antibodies
605 against TOPORS, CCAR1 and Golgi markers GM130 (cis-Golgi) and TGN46 (trans-Golgi);
606 scale bar, 1 μm; (B-D) white lines across the stack depict the line-plot analysis.
607 (**E**) Quantification of Pearson's correlation coefficient (PCC) between cis-Golgi and trans-
608 Golgi markers and DDR proteins; n ≥ 36 mini-stacks.
609 (**F**) Localisation changes of dual-localising DDR proteins upon induction of DNA damage.
610 HeLa-K cells were treated with the DNA damage-inducing drug, doxorubicin (DOX) (40 μM,
611 3 h) or oxidative stress-inducing agent hydrogen peroxide (H2O2) (50 μM for 20 min, followed
612 with 15 min recovery), fixed and stained with antibodies against DDR proteins LIG1, POLQ,
613 CCAR1 and the Golgi marker, GM130; yellow arrows denote the Golgi membranes. Scale
614 bars, 10 μm.
615 (**G**) A ratio of DDR protein Golgi-nuclear distribution after treatment with DOX.
616 (**H**) A ratio of DDR protein Golgi-nuclear distribution after treatment with H_2O_2. Data represent
617 the mean ± standard error of the mean (s.e.m.) ($n = 3$ biologically independent samples with
618 at least 200 cells analysed for each protein in control and treatment conditions). The proteins
619 are classified according to their Golgi localisation patterns **(E)**. Statistical significance was

determined using a two-tailed unpaired Student's *t*-test; ns, **P < 0.01, ***P < 0.001, ****P <0.0001, compared to untreated control.

Figure 3: Redistribution of RAD51C Golgi fraction is required for the formation of RAD51C nuclear foci and is dependent on the kinase ATM

(**A**) Representative images of HeLa-K, U-2 OS and MCF7 cells stained with antibodies against RAD51C (green) and GM130 (red). DNA stained with Hoechst 33342 (blue).

(**B**) Quantification of RAD51C distribution across the Golgi, nucleus and cytoplasm in various cell lines quantified from immunofluorescence images.

(**C**) WB analysis showing the subcellular membrane (M), nuclear (N) and cytoplasmic (C) fractions of RAD51C (markers: GM130 for Golgi membranes, Lamin B1 for the nuclear compartment, alpha-tubulin for the cytoplasmic fraction).

(**D**) Quantification of western blot analysis showing the distribution of RAD51C in 3 cell fractions: membrane, nuclear and cytoplasmic; ($n = 3$ biologically independent experiments) data represent the mean ± s.e.m.

(**E**) HeLa-K cells treated with the DNA damage-inducing drug, doxorubicin (DOX), for increasing lengths of time. Yellow arrows denote the Golgi membrane; white arrows denote nuclear foci.

(**F**) Quantification of sum intensity of RAD51C Golgi population, (**G**) RAD51C nuclear population, and (**H**) a ratio of RAD51C Golgi-nuclear distribution after treatment with DOX. Data represent the s.e.m ($n = 3$ biologically independent samples with a total of 2343 cells analysed).

(**I**) Quantification of RAD51C membrane-nuclear distribution ratio after treatment with DOX, calculated from isolated fractions (**Figure S6E**). HeLa-K cells were stained with antibodies against RAD51C and GM130.

(**J**) Cells were treated with DMSO or IPZ prior to a 3-hour treatment with DOX. Yellow arrows denote the Golgi membrane; white denote nuclear foci. Results were quantified as (**K**) ratio of RAD51C Golgi-nuclear distribution and (**L**) relative sum intensity of RAD51C at the Golgi Data represents s.e.m. ($n = 3$ biologically independent samples with a total of 445 cells analysed).

(**M**) HeLa-K cells were treated with DMSO (control) alone or with ATM inhibitor (KU55933) or ATR inhibitor (VE-821) or DNA-PK inhibitor (NU7441) prior to a 3-hour treatment with doxorubicin. Results were quantified as (**N**) ratio of RAD51C Golgi-nuclear distribution and (**O**) relative sum intensity of RAD51C at the Golgi. Data represents s.e.m. ($n = 3$ biologically independent samples with a total of 1679 cells analysed). Scale bars, 10 μm. Statistical significance was determined using a two-tailed unpaired Student's *t*-test.

Figure 4: RAD51C Golgi localisation is dependent on the Golgin protein, Giantin

(**A**) Schematic diagram highlighting the domain organisation of Giantin.

(**B**) RAD51C protein redistribution upon depletion of Giantin. HeLa-K cells were transfected with either control or Giantin siRNAs for 72 h, then immunostained for RAD51C and the Golgi marker GM130. Yellow arrows mark the Golgi, and white arrows denote RAD51C nuclear foci.

(**C–E**) Quantifications of RAD51C localisation: **(C)** total Golgi-associated RAD51C intensity, (**D**) the Golgi-to-nucleus RAD51C intensity ratio, and (**E**) the number of nuclear RAD51C foci per cell. Data are presented as mean ± s.e.m. (n = 3 biologically independent experiments, 1,445 total cells).

667 (**F**) Golgi-cisternal co-localisation analysis. HeLa-K cells treated with Nocodazole (33 μM, 3
668 h), fixed and stained with antibodies against Giantin and RAD51C.
669 (**G**) Zoom enlarged view of single isolated mini-stack; scale bar, 1 μm; white line across the
670 stack was used for line-scan analysis.
671 (**H and I**) Co-immunoprecipitation (co-IP) of endogenous Giantin with RAD51C under control
672 conditions (**H**) or after doxorubicin (DOX) treatment and co-treatments with ATM inhibitor
673 (ATMi) and importazole (IPZ) (**I**) in HeLa-K extracts.
674 (**J**–**M**) Co-localisation experiment of cells treated with control siRNA, or Giantin siRNA under
675 control conditional or after treatment with ETO. Cells stained with antibodies against RAD51C
676 (green) and HR DDR markers (red): (**J**) γ-H2AX, and (**L**) p-ATM. Co-localisation of structure
677 is denoted by an arrowhead. Quantification of percentage RAD51C foci co-localising with (**K**)
678 γ-H2AX and (**M**) p-ATM. Data represent the mean ± s.e.m. ($n = 3$ biologically independent
679 samples with at least 200 cells and at least 550 RAD51C nuclear foci analysed for the co-
680 localisation experiments for each condition).
681
682 **Figure 5: Depletion of Giantin leads to genomic instability, inhibition of DDR signalling**
683 **and accelerated cell proliferation**
684 (**A–C**) Representative images and associated quantification of micronuclei formation
685 following siRNA treatment under (**B**) basal condition and (**C**) after etoposide-induction DNA
686 damage (10 μM; 16 h followed by 6 h recovery); yellow arrows denote micronuclei structures.
687 Data represent the mean ± s.e.m. ($n = 3$ biologically independent samples with >10,000 cell
688 analysed).
689 (**D**) Representative comet assay images measuring genomic DNA fragmentation in HeLa-K
690 cells treated with control, Giantin, or RAD51C targeting siRNA.
691 (**E**) Quantification of OliveMoment from comet assay. Data represent the mean ± s.e.m. ($n = 3$
692 biologically independent samples).
693 (**F**–**I**) Representative colony formation assays in (**F**) HeLa-K and (**H**) U-2 OS cell lines with
694 corresponding quantification of colony area coverage in (**G**) HeLa-K and (**H**) U-2 OS cells.
695 Statistical significance was determined using a two-tailed unpaired Student's t-test. Scale
696 bars, 10 μm.
697 (**J**) WB analysis of HeLa-K cells transfected with control and Giantin siRNA and treated with
698 DOX (40 μM; 3 h). Extracts were prepared and immunoblotted as indicated ($n = 2$ biologically
699 independent samples).
700 (**K**) WB of HeLa-K cells treated with DOX (40 μM; 3 h) and IPZ (20 μM; 3 h).
701 (**L**) WB of HeLa-K cells transfected with siRNAs against Giantin, RAD51C or a combination
702 of both followed by treatment with DMSO, DOX (40 μM; 3h) or ETO (10 μM; 3 h) (M) with
703 associated quantification showing the relative levels of pATM; (n=3 biological independent
704 experiments), data represent the mean ± s.e.m.
705 (**N and O**) Quantification of micronuclei formation and fold change in cell number after siRNA
706 treatments (mean ± s.e.m., n = 3, ≥1,000 cells per condition).
707 (**P**) Proposed model for the regulation of HR-mediated repair through the activation of
708 RAD51C at the Golgi complex. RAD51C, a regulatory HR protein, is anchored to the Golgi
709 through its interaction with the cytoplasmic tail of Giantin, in response to double-strand DNA
710 breaks, this RAD51C Golgi population redistributes to form nuclear foci. This response
711 requires Importin-beta-mediated nuclear import and the phosphorylation of ATM protein
712 kinase. We propose that the Golgi functions as a spatiotemporal timing module that gates
713 RAD51C (and other DDR factors) availability to ensure proper homologous recombination
714 and DNA-damage signaling.

715
716 **Figure S1: Validation of DDR protein antibody specificity and localisation, related to**
717 **Figure 1**
718 Representative images of HeLa-K cells stained with antibodies against DDR proteins and the
719 Golgi marker, GM130. Cells were treated with a control or an siRNA against the protein of
720 interest to validate the specificity of the antibody. The changes in intensity measurements in
721 the Golgi and nuclear compartment were quantified (n=2 for all proteins except for POLQ,
722 which had n=1, biological independent samples with at least 500 cells analysed for each
723 treatment). Scale bar, 10 µm. Continued on **Figure S2A**.
724
725 **Figure S2: Validation of DDR protein localisation and functional network analysis,**
726 **related to Figure 1**
727 (**A**) Representative images of HeLa-K cells stained with antibodies against DDR proteins and
728 the Golgi marker, GM130. Cells were treated with a control or an siRNA against the protein
729 of interest to validate the specificity of the antibody. The changes in intensity measurements
730 in the Golgi and nuclear compartment were quantified. (n=2, biological independent samples
731 with at least 500 cells analysed for each treatment).
732 (**B**) Experimentally-based protein-protein interaction networks displaying the Golgi-nuclear
733 localisation proteins validated in this study. Proteins are categorised by functional pathways
734 annotated using gene ontology terms (**Table S1**).
735
736 **Figure S3: DOX-Induced Redistribution and Golgi-cisternal localisation analysis of**
737 **DDR proteins, related to Figure 2**
738 **(A)** Representative images of HeLa-K cells stained with antibodies against DDR proteins
739 (green) and the Golgi marker, GM130 (red). Cells were treated with DOX (40 µM, 3 h), fixed,
740 and immunostained. Yellow arrows denote Golgi membranes. Scale bars, 10 µm.
741 **(B and C)** Quantification of DDR protein intensity changes upon DOX treatment. **(B)** Relative
742 intensity of DDR proteins at the Golgi and **(C)** in the nucleus, normalised to untreated control.
743 Data represent the mean ± s.e.m. (*n* = 3 biologically independent samples with at least 200
744 cells analysed for each protein in control and treatment conditions). The proteins are
745 classified according to their Golgi localisation patterns (**Figure 2E**). Statistical significance
746 was determined using a two-tailed unpaired Student's *t*-test; ns P > 0.05, *P < 0.05, **P <
747 0.01, ***P < 0.001, ****P <0.0001, compared to untreated control.
748 (**D**) Golgi-cisternal localisation analysis of Golgi-nuclear DDR proteins. HeLa-K cells were
749 treated with Nocodazole (33 µM, 3 h), fixed and stained with antibodies against DDR
750 proteins. Quantification of Pearson's correlation coefficient (PCC) between *cis*-Golgi and
751 *trans*-Golgi markers and DDR proteins; N ≥ 4 cells; n ≥ 36 mini stacks.
752
753 **Figure S4**: **H_2O_2-Induced redistribution of DDR proteins, related to Figure 2**
754 (**A**) Representative images of HeLa-K cells were stained with antibodies against DDR
755 proteins and the Golgi marker, GM130. HeLa-K cells were treated with H_2O_2 (50 µM, for 20
756 min followed by 15 min recovery), fixed and stained with antibodies against DDR proteins
757 and the Golgi marker, GM130; yellow arrows denote the Golgi membranes. Scale bars, 10
758 µm.
759 **(B and C)** Quantification of DDR protein intensity changes upon H_2O_2 treatment. **(B)** Relative
760 intensity of DDR proteins at the Golgi and **(C)** in the nucleus, normalised to untreated control.
761 Data represent the mean ± s.e.m. (n = 3 biologically independent samples with at least 200

762 cells analysed for each protein in control and treatment conditions). The proteins are
763 classified according to their Golgi localisation patterns **(Figure 2E)**. Statistical significance
764 was determined using a two-tailed unpaired Student's t-test; ns P > 0.05, *P < 0.05 ***P <
765 0.001, ****P <0.0001, compared to untreated control.
766
767 **Figure S5: $KBrO_3$-Induced redistribution of DDR proteins, related to Figure 2**
768 (**A**) Representative images of HeLa-K cells were stained with antibodies against DDR
769 proteins and the Golgi marker, GM130. HeLa-K cells were treated with $KBrO_3$ (5 mM, 3h),
770 fixed and stained with antibodies against DDR proteins and the Golgi marker, GM130 (A to
771 D); yellow arrows denote the Golgi membranes. Scale bars, 10 µm.
772 **(B)** A ratio of DDR protein Golgi-nuclear distribution after treatment with $KBrO_3$.
773 (**C and D**) Quantification of DDR protein intensity changes upon $KBrO_3$ treatment. **(C)**
774 Relative intensity of DDR proteins at the Golgi and **(D)** in the nucleus, normalised to untreated
775 control. Data represent the mean ± s.e.m. (n = 3 biologically independent samples with at
776 least 200 cells analysed for each protein in control and treatment conditions). The proteins
777 are classified according to their Golgi localisation patterns **(Figure 2E)**. Statistical
778 significance was determined using a two-tailed unpaired Student's t-test; ns P > 0.05, *P <
779 0.05, **P < 0.01, ***P < 0.001, ****P <0.0001, compared to untreated control.
780
781 **Figure S6**: **Validation of RAD51C subcellular localisation, related to Figure 3**
782 (**A**) Representative images showing the RAD51C antibody specificity. HeLa-K cells were
783 stained with antibodies against RAD51C and GM130; DNA was stained with Hoechst 33342.
784 Scale bar, 10 µm.
785 (**B**) Quantification of RAD51C sum intensity after RAD51C depletion. Data represent the
786 mean ± s.e.m. (n = 3 biologically independent samples with a total of 831 cells analysed). (**C**)
787 Western blot analysis showing the level of RAD51C protein level, in RAD51C-depleted and
788 control cells (n = 3 biologically independent samples). Statistical significance was determined
789 using a two-tailed unpaired Student's t-test.
790 (**D**) Western blot analysis showing the subcellular localisation of RAD51C treated with the
791 DMSO and doxorubicin. The protein levels normalised against the respective fraction control
792 ($RAD51C^{mem}$/GM130; $RAD51C^{nuc}$/Lamin B1; $RAD51C^{cyt}$/tubulin). Data represent the
793 mean ± s.e.m; (n = 2 biologically independent samples).
794 (**E**) Quantification of RAD51C membrane-nuclear distribution ratio after treatment with DOX,
795 calculated from isolated fractions.
796
797 **Figure S7: RAD51C Golgi population redistribution upon treatment with IPZ and**
798 **inhibition of DDR signalling, related to Figure 3**
799 **(A)** Representative images of the RAD51C protein redistribution upon treatment with IPZ and
800 DOX. HeLa-K cells were stained with antibodies against RAD51C and GM130. Cells were
801 treated with DMSO or IPZ prior to a 3-hour treatment with DOX.
802 (**B**) Representative images of the RAD51C protein redistribution upon treatment with DDR
803 signalling inhibitors and DOX. HeLa-K cells were treated with DMSO (control) alone or with
804 ATM inhibitor (KU55933), ATR inhibitor (VE-821) or DNA-PK inhibitor (NU7441) prior to a 3-
805 hour treatment with doxorubicin. Yellow arrows denote the Golgi membrane; white denotes
806 nuclear foci. Scale bars, 10 µm.
807
808 **Figure S8**: **RAD51C protein localisation and redistribution upon induction treatment**
809 **with DNA damage agents, related to Figure 3**

(A) Representative images of HeLa-K cells stained with antibodies against RAD51C and GM130 after treatment with Camptothecin (CPT) for 16 h followed by media change for 2 h. Scale bar, 10 µm.
(B) Quantification of RAD51C distribution between the Golgi and nuclear compartments after CPT treatment.
(C) Quantification of RAD51C distribution ratio between the Golgi and nuclear compartments after CPT treatment.
(D) Representative images of HeLa-K cells stained with antibodies against RAD51C and GM130 after treatment with Etoposide (ETO) for 16 hours followed by media change for 2 h. Scale bar, 10 µm.
(E) Quantification of RAD51C distribution between the Golgi and nuclear compartments after ETO treatment.
(F) Quantification of RAD51C distribution ratio between the Golgi and nuclear compartments after ETO treatment.
(G) Representative images of HeLa-K cells stained with antibodies against RAD51C and GM130 after treatment with Mitomycin C (MMC)for 16 h followed by media change for 2 h. Scale bar, 10 µm.
(H) Quantification of RAD51C distribution between the Golgi and nuclear compartments after MMC treatment.
(I) Quantification of RAD51C distribution ratio between the Golgi and nuclear compartments after ETO treatment.
Data represent the mean ± s.e.m. (n = 3 biologically independent samples with more than 600 cells analyzed per treatment). Statistical significance was determined using a two-tailed unpaired Student's t-test. **P < 0.01; ***P < 0.001.

Figure S9: Impact of Golgin proteins on DNA repair, cell cycle, and breast cancer survival, related to Figure 4 and Figure 5
(**A**) Re-analysed siRNA screen data (Adamson et al. 2012) showing the relative Homologous Recombination (HR) repair rate upon systematic knockdown of the Golgin protein family (grey) and HR complex proteins (black).
(**B**) Re-analysed siRNA screen data (Paulsen 2010) showing the relative percent cell population with phosphorylation of H2AX upon systematic knockdown of the Golgins. The datasets are normalised to the negative control set at 1.
(**C**) HeLa-K cells were transfected with control, or Giantin siRNAs for 72 hours. The cells were stained with antibodies against Giantin and nuclei were stained with Hoechst 33342. Scale bar, 10 µm.
(**D**) Cell cycle profile of HeLa-K cell treated with Giantin or control siRNA. Data represent the mean ± s.e.m. (*n* = 3 biologically independent samples).
(**E and F**) Kaplan-Meier survival plots in patients with high and low mRNA **(F)** (Győrffy 2021) and protein (**G**) (Ősz, Lánczky, and Győrffy 2021) Giantin expression in Breast Cancer patients. The graph was generated using the kmplot database (https://kmplot.com).

Supplementary Table S1. Set of tables listing the antibodies and siRNA used for the analysis of Human Protein Atlas dataset for the identification and validation of dual-localising Golgi-nuclear proteins. Table 1 presents the antibodies and siRNA used; Table 2 presents the identified and validated Golgi-nuclear protein. Table 3 presents the gene ontology and enrichment terms of the validated Golgi-nuclear proteins.

858 **Supplementary Table S2.** Table listing the cross-correlation measure for analysis of Golgi
859 cisternal localisation analysis of dual-localising DDR proteins.
860
861
862 **Materials and Methods**
863
864 **Antibodies and chemicals.** Several commercially antibodies and chemical were used in the
865 paper, including RAD51C (ab72063, Abcam; 1:500 for immunostaining) & (ab95069, Abcam,
866 1:2000 for western blotting; 1:500 for immunoprecipitation), GOLGB1/Giantin (AF8159, R&D
867 systems; 1:500 for immunostaining and immunoprecipitation, 1:2000 for western blotting) &
868 (G1/M1, Enzo Life Sciences, 1:500 for immunostaining), GM130 (610822, BD Biosciences;
869 1:500 for immunostaining, 1:2000 for western blotting), TGN46 (AHP500GT, Bio-Rad; 1:1000
870 for immunostaining; 1:2000 for western blotting), ATM (MA1-23152, Invitrogen; 1:2000 for
871 western blotting), pATM Ser1981 (MA1-2020, Invitrogen; 1:500 for immunostaining; 1:2000
872 for western blotting), CHK2 pThr68 (PA5-17818, Invitrogen; 1:2000 for western blotting),
873 DNA-PKcs (Ser2056) (PA5-78130, Invitrogen, 1:2000 for western blotting), gamma-H2AX
874 pSer139 (613402, Biolegend; 1:500 for immunostaining, 1:2000 for western blotting), alpha-
875 tubulin (MS-581, Thermo Fisher; 1:10,000 for western blotting) Lamin B1 (ab16048, Abcam;
876 1:2000 for western blotting), doxorubicin (ab120629, Abcam); Importazole (SML0341,
877 Sigma-Aldrich), KU55933 (ATMi, SML1109, Sigma-Aldrich); ve-821 (ATRi, HY-14731;
878 MedChemExpress) NU7441 (DNA-PKi, HY-11006; MedChemExpress), etoposide
879 (ab120227, Abcam), mitomycin C (M7949, Sigma-Aldrich), hydrogen peroxide (H1009,
880 Sigma-Aldrich), potassium bromate (104912, Merck Millipore), camptothecin (ab120115,
881 Abcam), SYBR Gold (S11494, Invitrogen), crystal violet (C0775-100G, Sigma-Aldrich).
882
883 **Cell lines, cell culture and siRNA transfection.** HeLa Kyoto, U-2 OS, MCF7, were cultured
884 in DMEM (Life Technologies) supplemented with 10% FBS (Invitrogen) and 1% L-glutamine
885 (Invitrogen). Cells were checked for mycoplasma contamination by PCR. siRNA transfections
886 were performed with Lipofectamine 2000 (Invitrogen) using SilencerSelect siRNAs (Ambion)
887 according to the manufacturer's instructions. Transfections were carried out for 72 h and the
888 final siRNA concentrations used were 15nM for all siRNAs. Giantin siRNA-1: 5951 & siRNA-
889 2: 5953; GMAP210 siRNA-1: s17811 & siRNA-2: s17812; RAD51C siRNA: s11737.
890
891 **Localisation validation siRNA assay**. A custom-designed siRNA library targeting our
892 proteins of interest (Ambion) was designed and prepared in 96-well glass bottom plates
893 (Miltenyi Biotec) using a protocol for solid phase reverse transfection as previously described
894 (Erfle et al. 2008; Stadler et al. 2012). Non-targeting siRNA was used as a negative control.
895 72 hours after cell seeding, cells were fixed with 4% paraformaldehyde (PFA), permeabilised
896 with 0.1% Triton-X100 and immunostained against the HPA antibodies of interest and a Golgi
897 marker, GM130. Hoechst 33342 was used as a nuclear stain. siRNAs and antibodies details
898 are available in Supplementary Table S1. Images were acquired on a fully automated
899 Molecular Devices IXM with a 10x/0.45 NA P-APO objective. The resulting images were
900 analysed using Cell Profiler software (Carpenter et al. 2006) for quantitative and automated
901 measurements of fluorescence from the antibodies as previously described (Stadler et al.
902 2012). Briefly, nuclei were segmented in the nuclear channel, the Golgi complex was
903 segmented in the Golgi marker channel and using the segmented nuclei as seeds, the two
904 structures were associated. Intensity profiles of each compartment were acquired. A
905 reduction of 25% or more of the antibody staining in both Golgi and nuclear compartments

906 was considered as a validation of the antibody specificity **(Figures S1 and S2;**
907 **Supplementary Table S1)**.
908
909 **Golgi cisternal localisation analysis.** As previously described (Dejgaard et al. 2007),
910 HeLa-K cells were treated with nocodazole (33 μM) or the solvent control methanol for 3 h.
911 After treatment, cells were fixed with 4% PFA, permeabilized with 0.1% Triton-X100 and
912 immunostained using antibodies against *trans*-Golgi marker, TGN46, *cis*-Golgi marker,
913 GM130 and the protein of interest. Images of the Golgi mini-stacks were acquired using a
914 confocal microscope Olympus Fluoview FV3000 with a 60x/1.3 NA silicon oil immersion
915 apochromatic objective. Golgi mini-stacks were visually inspected, and those that were in the
916 same plane were selected for analysis. Images were analysed using Fiji (Schindelin et al.
917 2012); the relative position of the fluorescence profile of the protein of interest against the
918 *trans*- and *cis-Golgi* markers was measured using a plot profile tool. The measured distances
919 were used to calculate Pearson's correlation coefficient (PCC) between *cis*-Golgi and *trans*-
920 Golgi markers and proteins of interest.
921
922 **Drug treatments.** Cells were treated 24 h after seeding. For camptothecin, etoposide and
923 mitomycin C experiments, cells were treated for 16 h at a concentration of 0.1 μM, 50 μM
924 and 5 μM, respectively. After treatment cells were incubated with fresh medium for 2 hours.
925 H_2O_2 experiments were performed by treating cells for 20 min at a concentration of 50 μM,
926 followed by change with fresh medium and 15 min recovery. For nocodazole and $KBrO_3$
927 experiments cells were treated for 3 h at the concentration of 33 μM and 5 mM, respectively.
928 Doxorubicin was used at a concentration of 40 μM for 3 h unless indicated otherwise. For
929 kinase and importin-β inhibitor treatments, cells were pretreated for 30 min with the described
930 inhibitor prior to the addition of doxorubicin. The inhibitors were used at the following
931 concentrations: importazole (IPZ) (20 μM), KU55933 (ATMi) (30 μM), NU7441 (DNA-Pki) (10
932 μM) and ve-821 (ATRi) (10 μM).
933
934 **Immunofluorescence assay.** Cells were fixed with 4% paraformaldehyde in PBS and
935 permeabilised with 0.1% Triton X-100 for 15 min at room temperature, then cells were
936 blocked with 5% bovine serum albumin in 0.05% Triton X-100 for 60 min and incubated with
937 primary antibodies in blocking buffer at room temperature for 3 h. Following 3 washes with
938 PBS, cells were incubated with fluorescent dye-conjugated secondary antibodies diluted in
939 a blocking buffer for 1 h at room temperature.
940
941 **Image and data analysis.** Confocal microscopy experiments were performed with fixed and
942 immunostained cell samples on a microscope FV3000, Olympus. Z stacks of images
943 covering the entire cell thickness were acquired. All image analysis was performed using Cell
944 Profiler (Carpenter et al. 2006) and Fiji (Schindelin et al. 2012). Briefly, first nuclei were
945 segmented in the Hoechst channel. When appropriate, the Golgi complex was segmented in
946 the Golgi marker channel and using the segmented nuclei as seeds, the two structures were
947 associated. Intensity profiles, morphology features and structuring counting analysis were
948 performed when required using Cell Profiler.
949
950 **Comet assay.** The assay was carried out as previously described (Vodenkova et al. 2020).
951 Briefly, cells were trypsinised, pelletised and resuspended in ice-cold PBS at a concentration
952 of 25×10^4 cells per ml. The cells were resuspended in 2% low melting agarose (Sigma) and
953 spread quickly onto gel bond film (Biozym) covered in 1% agarose (Sigma). Samples were

954 immersed into a lysis buffer (100 mM EDTA, 2.5 M NaCl, 10 mM Tris-HCl and 1% Triton-
955 X100; pH 10) overnight at 4°C. Followed by a wash with ice-cold water and run in an
956 electrophoresis chamber (alkaline buffer: 1 mM EDTA, 300 mM NaOH; pH 13) at 15 V, 300
957 mA for 60 min at 4°C. Slides were first washed in a Tris-HCl neutralisation buffer (0.4 M; pH
958 7.5) followed by water, stained with SYBR Gold (Thermo Fisher Scientific) (1:10000) and
959 finally dried. Comets were imaged by an automated Olympus Scan^R screening microscope
960 and comet tails were scored using OpenComet plugin (Gyori et al. 2014).
961
962 **Western blotting analysis.** HeLa-K cells were lysed using RIPA buffer (Thermo Scientific)
963 with a complete protease inhibitor cocktail (Roche). SDS-PAGE was performed on pre-cast
964 Tris-Acetate gels followed by transfer to PVDF transfer membrane (Merck Millipore). Proteins
965 were detected using primary antibodies as described followed by incubation with secondary
966 antibodies coupled with HRP (Invitrogen). Detection of protein was performed using Pierce
967 ECL Plus Western Blotting Substrate reagent (Thermo Scientific) and visualised on Azure
968 280 chemiluminescent imaging system. Golgi enrichment assay was performed using
969 Minute™ Golgi Apparatus Enrichment Kit (GO-037, Invent Biotechnologies) according to the
970 manufacturer's instructions. The purity of the cis and trans-Golgi fractions was confirmed by
971 using Golgi markers GM130 for the *cis*-Golgi and TGN-46 for the *trans*-Golgi. Subcellular
972 fractionation was performed using a subcellular protein fractionation kit for cultured cells
973 (78840, Thermo Scientific) according to the manufacturer's instructions. Fractions were
974 verified using well-established markers (GM130 for Golgi membranes, Lamin B1 for the
975 nuclear compartment, and alpha-tubulin for the cytoplasmic fraction) and probed for proteins
976 of interest presence in each compartment. Protein membrane:nuclear distribution ratio was
977 calculated by first dividing the protein level in each fraction by the protein level of the
978 appropriate control, the resulting membrane ($M_{protein}$ / M_{GM130}) and nuclear ($N_{protein}$ / $N_{laminB1}$)
979 ratios were further divided to give the ratio = ($M_{protein}$ / M_{GM130}) / ($N_{protein}$ / $N_{laminB1}$). The ratios
980 obtained from the control were normalised to 1 and compared to the treated group.
981
982 **Immunoprecipitation.** HeLa-K cells were lysed using a lysis buffer (50 mM Hepes, 130 mM
983 NaCl, 1 mM DTT 1% NP-40) with a complete protease inhibitor cocktail (Roche). Cell lysates
984 were centrifuged at 13,000 rpm for 10 mins at 4°C. For immunoprecipitation, the lysates were
985 incubated with the primary antibody described and rotated overnight at 4°C. Next, the lysates
986 were incubated with G-agarose beads (Roche) and rotated for 4 h at 4°C. The samples were
987 washed with cold lysis buffer and then precipitated proteins were eluted by 2x SDS sample
988 buffer and analysed by Western blotting.
989
990 **Colony formation assay.** HeLa-K or U-2 OS cells, transfected with either a Giantin or control
991 siRNA were seeded on a 6-well plate (500 cells/well) and allowed to grow for 12 days in a
992 complete culture medium. Where indicated, 24h after seeding the cells were treated with a
993 DNA damaging agent, DOX (1 μM) or a solvent control, DMSO for 24h. Subsequently, the
994 medium was replaced, and it was refreshed every 4 days. The resulting colonies were
995 washed twice with PBS, followed by fixing and staining for 30 min with a solution containing
996 0.1% (w/v) crystal violet and 20% (v/v) ethanol. Then the colonies were washed again to
997 remove excess crystal violet with PBS. Finally, after the dishes were dry, digital images of
998 the colonies were acquired using a camera and quantified.
999
1000 **Statistical analysis.** All data were obtained from at least three independent experiments if
1001 not otherwise stated. Statistical analyses were performed using a two-tailed t-test for pairwise

comparison and one-way analysis of variance (ANOVA) for multiple comparisons on GraphPad Prism 9. Data are expressed as the standard error of the mean (s.e.m.). n values indicate biologically independent samples and experiments. $P < 0.05$ was considered statistically significant.

Acknowledgements. We thank the ALMF, FCCF and the Pepperkok team for their support. In addition, we acknowledge Jan Ellenberg, Claudia Lukas, Alba Diz-Muñoz, Diana Ordonez, Per Haberkant and Simone Köhler for their assistance in developing the project and manuscript. G.G. was supported by the EMBL EIPOD programme, K.K. by the EMBL PhD programme and M.M.K. by the German Centre for Lung Research.

References:

Adamson, Britt, Agata Smogorzewska, Frederic D. Sigoillot, Randall W. King, and Stephen J. Elledge. 2012. “A Genome-Wide Homologous Recombination Screen Identifies the RNA-Binding Protein RBMX as a Component of the DNA-Damage Response.” *Nature Cell Biology* 14 (3): 318–28.

Badie, Sophie, Chunyan Liao, Maria Thanasoula, Paul Barber, Mark A. Hill, and Madalena Tarsounas. 2009. “RAD51C Facilitates Checkpoint Signaling by Promoting CHK2 Phosphorylation.” *The Journal of Cell Biology* 185 (4): 587–600.

Baschieri, Francesco, Edith Uetz-von Allmen, Daniel F. Legler, and Hesso Farhan. 2015. “Loss of GM130 in Breast Cancer Cells and Its Effects on Cell Migration, Invasion and Polarity.” *Cell Cycle* 14 (8): 1139–47.

Berti, Matteo, Federico Teloni, Sofija Mijic, Sebastian Ursich, Jevgenij Fuchs, Maria Dilia Palumbieri, Jana Krietsch, et al. 2020. “Sequential Role of RAD51 Paralog Complexes in Replication Fork Remodeling and Restart.” *Nature Communications* 11 (1): 3531.

Bhat, Ganapati, Vishwanath-Reddy Hothpet, Ming-Fong Lin, and Pi-Wan Cheng. 2017. “Shifted Golgi Targeting of Glycosyltransferases and α-Mannosidase IA from Giantin to GM130-GRASP65 Results in Formation of High Mannose N-Glycans in Aggressive Prostate Cancer Cells.” *Biochimica et Biophysica Acta (BBA) - General Subjects* 1861 (11, Part A): 2891–2901.

Brown, Michael S., Arun Radhakrishnan, and Joseph L. Goldstein. 2018. “Retrospective on Cholesterol Homeostasis: The Central Role of Scap.” *Annual Review of Biochemistry* 87 (June):783–807.

Bui, Sarah, Isabel Mejia, Begoña Díaz, and Yanzhuang Wang. 2021. “Adaptation of the Golgi Apparatus in Cancer Cell Invasion and Metastasis.” *Frontiers in Cell and Developmental Biology* 9 (December):806482.

Carpenter, Anne E., Thouis R. Jones, Michael R. Lamprecht, Colin Clarke, In Han Kang, Ola Friman, David A. Guertin, et al. 2006. “CellProfiler: Image Analysis Software for Identifying and Quantifying Cell Phenotypes.” *Genome Biology* 7 (10): R100.

Ciccia, Alberto, and Stephen J. Elledge. 2010. “The DNA Damage Response: Making It Safe to Play with Knives.” *Molecular Cell* 40 (2): 179–204.

Craven, Kelly E., Yesim Gökmen-Polar, and Sunil S. Badve. 2021. “CIBERSORT Analysis of TCGA and METABRIC Identifies Subgroups with Better Outcomes in Triple Negative Breast Cancer.” *Scientific Reports* 11 (1): 4691.

Dejgaard, Selma Yilmaz, Ayesha Murshid, Kristina M. Dee, and John F. Presley. 2007. “Confocal Microscopy-Based Linescan Methodologies for Intra-Golgi Localization of Proteins.” *The Journal of Histochemistry and Cytochemistry: Official Journal of the Histochemistry Society* 55 (7): 709–19.

Erfle, Holger, Beate Neumann, Phill Rogers, Jutta Bulkescher, Jan Ellenberg, and Rainer Pepperkok. 2008. “Work Flow for Multiplexing siRNA Assays by Solid-Phase Reverse

1053 Transfection in Multiwell Plates." *Journal of Biomolecular Screening* 13 (7): 575–80.
1054 Farber-Katz, Suzette E., Holly C. Dippold, Matthew D. Buschman, Marshall C. Peterman,
1055 Mengke Xing, Christopher J. Noakes, John Tat, et al. 2014. "DNA Damage Triggers
1056 Golgi Dispersal via DNA-PK and GOLPH3." *Cell* 156 (3): 413–27.
1057 Feng, Zhihui, Lisa Kachnic, Junran Zhang, Simon N. Powell, and Fen Xia. 2004. "DNA
1058 Damage Induces p53-Dependent BRCA1 Nuclear Export*." *The Journal of Biological*
1059 *Chemistry* 279 (27): 28574–84.
1060 Fokas, E., R. Prevo, J. R. Pollard, P. M. Reaper, P. A. Charlton, B. Cornelissen, K. A.
1061 Vallis, et al. 2012. "Targeting ATR in Vivo Using the Novel Inhibitor VE-822 Results in
1062 Selective Sensitization of Pancreatic Tumors to Radiation." *Cell Death & Disease* 3
1063 (12): e441.
1064 Freeze, Hudson H., and Bobby G. Ng. 2011. "Golgi Glycosylation and Human Inherited
1065 Diseases." *Cold Spring Harbor Perspectives in Biology* 3 (9): a005371.
1066 Ghannoum, Salim, Damiano Fantini, Muhammad Zahoor, Veronika Reiterer, Santosh
1067 Phuyal, Waldir Leoncio Netto, Øystein Sørensen, et al. 2023. "A Combined
1068 Experimental-Computational Approach Uncovers a Role for the Golgi Matrix Protein
1069 Giantin in Breast Cancer Progression." *PLoS Computational Biology* 19 (4): e1010995.
1070 Greenhough, Luke A., Chih-Chao Liang, Ondrej Belan, Simone Kunzelmann, Sarah
1071 Maslen, Monica C. Rodrigo-Brenni, Roopesh Anand, Mark Skehel, Simon J. Boulton,
1072 and Stephen C. West. 2023. "Structure and Function of the RAD51B-RAD51C-
1073 RAD51D-XRCC2 Tumour Suppressor." *Nature* 619 (7970): 650–57.
1074 Győrffy, Balázs. 2021. "Survival Analysis across the Entire Transcriptome Identifies
1075 Biomarkers with the Highest Prognostic Power in Breast Cancer." *Computational and*
1076 *Structural Biotechnology Journal* 19 (July):4101–9.
1077 Gyori, Benjamin M., Gireedhar Venkatachalam, P. S. Thiagarajan, David Hsu, and Marie-
1078 Veronique Clement. 2014. "OpenComet: An Automated Tool for Comet Assay Image
1079 Analysis." *Redox Biology* 2 (January):457–65.
1080 Haze, K., H. Yoshida, H. Yanagi, T. Yura, and K. Mori. 1999. "Mammalian Transcription
1081 Factor ATF6 Is Synthesized as a Transmembrane Protein and Activated by Proteolysis
1082 in Response to Endoplasmic Reticulum Stress." *Molecular Biology of the Cell* 10 (11):
1083 3787–99.
1084 Henle, E. S., and S. Linn. 1997. "Formation, Prevention, and Repair of DNA Damage by
1085 Iron/hydrogen Peroxide." *The Journal of Biological Chemistry* 272 (31): 19095–98.
1086 Hickson, Ian, Yan Zhao, Caroline J. Richardson, Sharon J. Green, Niall M. B. Martin,
1087 Alisdair I. Orr, Philip M. Reaper, Stephen P. Jackson, Nicola J. Curtin, and Graeme C.
1088 M. Smith. 2004. "Identification and Characterization of a Novel and Specific Inhibitor of
1089 the Ataxia-Telangiectasia Mutated Kinase ATM." *Cancer Research* 64 (24): 9152–59.
1090 Jekimovs, Christian, Emma Bolderson, Amila Suraweera, Mark Adams, Kenneth J.
1091 O'Byrne, and Derek J. Richard. 2014. "Chemotherapeutic Compounds Targeting the
1092 DNA Double-Strand Break Repair Pathways: The Good, the Bad, and the Promising."
1093 *Frontiers in Oncology* 4 (April):86.
1094 Krupina, Ksenia, Alexander Goginashvili, and Don W. Cleveland. 2021. "Causes and
1095 Consequences of Micronuclei." *Current Opinion in Cell Biology* 70 (June):91–99.
1096 Kulkarni-Gosavi, Prajakta, Christian Makhoul, and Paul A. Gleeson. 2019. "Form and
1097 Function of the Golgi Apparatus: Scaffolds, Cytoskeleton and Signalling." *FEBS Letters*
1098 593 (17): 2289–2305.
1099 Leighton, Jake, Min Hu, Emi Sei, Funda Meric-Bernstam, and Nicholas E. Navin. 2023.
1100 "Reconstructing Mutational Lineages in Breast Cancer by Multi-Patient-Targeted
1101 Single-Cell DNA Sequencing." *Cell Genomics* 3 (1): 100215.
1102 Liu, Jianyang, Yan Huang, Ting Li, Zheng Jiang, Liuwang Zeng, and Zhiping Hu. 2021.
1103 "The Role of the Golgi Apparatus in Disease (Review)." *International Journal of*
1104 *Molecular Medicine* 47 (4). https://doi.org/10.3892/ijmm.2021.4871.
1105 Loft, S., X. S. Deng, J. Tuo, A. Wellejus, M. Sørensen, and H. E. Poulsen. 1998.
1106 "Experimental Study of Oxidative DNA Damage." *Free Radical Research* 29 (6): 525–
1107 39.

Machamer, Carolyn E. 2015. “The Golgi Complex in Stress and Death.” *Frontiers in Neuroscience* 9 (November):421.

Makhoul, Christian, Prajakta Gosavi, and Paul A. Gleeson. 2018. “The Golgi Architecture and Cell Sensing.” *Biochemical Society Transactions* 46 (5): 1063–72.

Mathioudaki, Argyri, Viktor Ljungström, Malin Melin, Maja Louise Arendt, Jessika Nordin, Åsa Karlsson, Eva Murén, et al. 2021. “Author Correction: Targeted Sequencing Reveals the Somatic Mutation Landscape in a Swedish Breast Cancer Cohort.” *Scientific Reports* 11 (1): 5310.

Miller, Kristi A., John M. Hinz, N. Alice Yamada, Lawrence H. Thompson, and Joanna S. Albala. 2005. “Nuclear Localization of Rad51B Is Independent of Rad51C and BRCA2.” *Mutagenesis* 20 (1): 57–63.

Møller, Peter. 2018. “The Comet Assay: Ready for 30 More Years.” *Mutagenesis* 33 (1): 1–7.

Ősz, Ágnes, András Lánczky, and Balázs Győrffy. 2021. “Survival Analysis in Breast Cancer Using Proteomic Data from Four Independent Datasets.” *Scientific Reports* 11 (1): 16787.

Ovejero, Sara, Sylvain Kumanski, Caroline Soulet, Julie Azarli, Benjamin Pardo, Olivier Santt, Angelos Constantinou, Philippe Pasero, and María Moriel-Carretero. 2023. “A Sterol-PI(4)P Exchanger Modulates the Tel1/ATM Axis of the DNA Damage Response.” *The EMBO Journal* 42 (15): e112684.

Paulsen, Renee Darlene. 2010. *A Genome-Wide SiRNA Screen Reveals Diverse Cellular Processes and Pathways That Mediate Genomic Stability*. Stanford University.

Petrosyan, Armen. 2015. “Onco-Golgi: Is Fragmentation a Gate to Cancer Progression?” *Biochemistry & Molecular Biology Journal* 1 (1). https://doi.org/10.21767/2471-8084.100006.

Pipek, Orsolya, Donát Alpár, Orsolya Rusz, Csaba Bödör, Zoltán Udvarnoki, Anna Medgyes-Horváth, István Csabai, et al. 2023. “Genomic Landscape of Normal and Breast Cancer Tissues in a Hungarian Pilot Cohort.” *International Journal of Molecular Sciences* 24 (10). https://doi.org/10.3390/ijms24108553.

Prakash, Rohit, Yashpal Rawal, Meghan R. Sullivan, Mckenzie K. Grundy, Hélène Bret, Michael J. Mihalevic, Hayley L. Rein, et al. 2022. “Homologous Recombination-Deficient Mutation Cluster in Tumor Suppressor RAD51C Identified by Comprehensive Analysis of Cancer Variants.” *Proceedings of the National Academy of Sciences of the United States of America* 119 (38): e2202727119.

Rawal, Yashpal, Lijia Jia, Aviv Meir, Shuo Zhou, Hardeep Kaur, Eliza A. Ruben, Youngho Kwon, et al. 2023. “Structural Insights into BCDX2 Complex Function in Homologous Recombination.” *Nature* 619 (7970): 640–49.

Rein, Hayley L., Kara A. Bernstein, and Robert A. Baldock. 2021. “RAD51 Paralog Function in Replicative DNA Damage and Tolerance.” *Current Opinion in Genetics & Development* 71 (December):86–91.

Rodriguez, José Antonio, Stefan Schüchner, Wendy W. Y. Au, Megan Fabbro, and Beric R. Henderson. 2004. “Nuclear-Cytoplasmic Shuttling of BARD1 Contributes to Its Proapoptotic Activity and Is Regulated by Dimerization with BRCA1.” *Oncogene* 23 (10): 1809–20.

Schindelin, Johannes, Ignacio Arganda-Carreras, Erwin Frise, Verena Kaynig, Mark Longair, Tobias Pietzsch, Stephan Preibisch, et al. 2012. “Fiji: An Open-Source Platform for Biological-Image Analysis.” *Nature Methods* 9 (7): 676–82.

Shiloh, Yosef, and Yael Ziv. 2013. “The ATM Protein Kinase: Regulating the Cellular Response to Genotoxic Stress, and More.” *Nature Reviews. Molecular Cell Biology* 14 (4): 197–210.

Soderholm, Jonathan F., Stephen L. Bird, Petr Kalab, Yasaswini Sampathkumar, Keisuke Hasegawa, Michael Uehara-Bingen, Karsten Weis, and Rebecca Heald. 2011. “Importazole, a Small Molecule Inhibitor of the Transport Receptor Importin-β.” *ACS Chemical Biology* 6 (7): 700–708.

Somyajit, Kumar, Sneha Saxena, Sharath Babu, Anup Mishra, and Ganesh Nagaraju.

1163 2015. “Mammalian RAD51 Paralogs Protect Nascent DNA at Stalled Forks and
1164 Mediate Replication Restart.” *Nucleic Acids Research* 43 (20): 9835–55.
1165 Somyajit, Kumar, Shreelakshmi Subramanya, and Ganesh Nagaraju. 2012. “Distinct Roles
1166 of FANCO/RAD51C Protein in DNA Damage Signaling and Repair.” *The Journal of*
1167 *Biological Chemistry* 287 (5): 3366–80.
1168 Stadler, Charlotte, Martin Hjelmare, Beate Neumann, Kalle Jonasson, Rainer Pepperkok,
1169 Mathias Uhlén, and Emma Lundberg. 2012. “Systematic Validation of Antibody Binding
1170 and Protein Subcellular Localization Using siRNA and Confocal Microscopy.” *Journal*
1171 *of Proteomics* 75 (7): 2236–51.
1172 Sullivan, Meghan R., and Kara A. Bernstein. 2018. “RAD-Ical New Insights into RAD51
1173 Regulation.” *Genes* 9 (12). https://doi.org/10.3390/genes9120629.
1174 Tavecchio, Michele, Joanne M. Munck, Celine Cano, David R. Newell, and Nicola J. Curtin.
1175 2012. “Further Characterisation of the Cellular Activity of the DNA-PK Inhibitor,
1176 NU7441, Reveals Potential Cross-Talk with Homologous Recombination.” *Cancer*
1177 *Chemotherapy and Pharmacology* 69 (1): 155–64.
1178 Thompson, Marilyn E. 2010. “BRCA1 16 Years Later: Nuclear Import and Export
1179 Processes.” *The FEBS Journal* 277 (15): 3072–78.
1180 Thorn, Caroline F., Connie Oshiro, Sharon Marsh, Tina Hernandez-Boussard, Howard
1181 McLeod, Teri E. Klein, and Russ B. Altman. 2011. “Doxorubicin Pathways:
1182 Pharmacodynamics and Adverse Effects.” *Pharmacogenetics and Genomics* 21 (7):
1183 440–46.
1184 Thul, Peter J., Lovisa Åkesson, Mikaela Wiking, Diana Mahdessian, Aikaterini Geladaki,
1185 Hammou Ait Blal, Tove Alm, et al. 2017. “A Subcellular Map of the Human Proteome.”
1186 *Science* 356 (6340). https://doi.org/10.1126/science.aal3321.
1187 Vítor, Alexandra C., Pablo Huertas, Gaëlle Legube, and Sérgio F. de Almeida. 2020.
1188 “Studying DNA Double-Strand Break Repair: An Ever-Growing Toolbox.” *Frontiers in*
1189 *Molecular Biosciences* 7 (February):24.
1190 Vodenkova, Sona, Amaya Azqueta, Andrew Collins, Maria Dusinska, Isabel Gaivão, Peter
1191 Møller, Alena Opattova, Pavel Vodicka, Roger W. L. Godschalk, and Sabine A. S.
1192 Langie. 2020. “An Optimized Comet-Based in Vitro DNA Repair Assay to Assess Base
1193 and Nucleotide Excision Repair Activity.” *Nature Protocols* 15 (12): 3844–78.
1194 Wang, Lingchen, Wenhua Wang, Shaopeng Zeng, Huilie Zheng, and Quqin Lu. 2020.
1195 “Construction and Validation of a 6-Gene Nomogram Discriminating Lung Metastasis
1196 Risk of Breast Cancer Patients.” *PloS One* 15 (12): e0244693.
1197 Wilson, Cathal, Rossella Venditti, Laura R. Rega, Antonino Colanzi, Giovanni D’Angelo,
1198 and M. Antonietta De Matteis. 2011. “The Golgi Apparatus: An Organelle with Multiple
1199 Complex Functions.” *Biochemical Journal* 433 (1): 1–9.
1200 Witkos, Tomasz M., and Martin Lowe. 2015. “The Golgin Family of Coiled-Coil Tethering
1201 Proteins.” *Frontiers in Cell and Developmental Biology* 3:86.
1202 Zappa, Francesca, Mario Failli, and Maria Antonietta De Matteis. 2018. “The Golgi
1203 Complex in Disease and Therapy.” *Current Opinion in Cell Biology* 50 (February):102–
1204 16.
1205 Zhang, Xiaoyan. 2021. “Alterations of Golgi Structural Proteins and Glycosylation Defects
1206 in Cancer.” *Frontiers in Cell and Developmental Biology* 9 (May):665289.

Figure 1

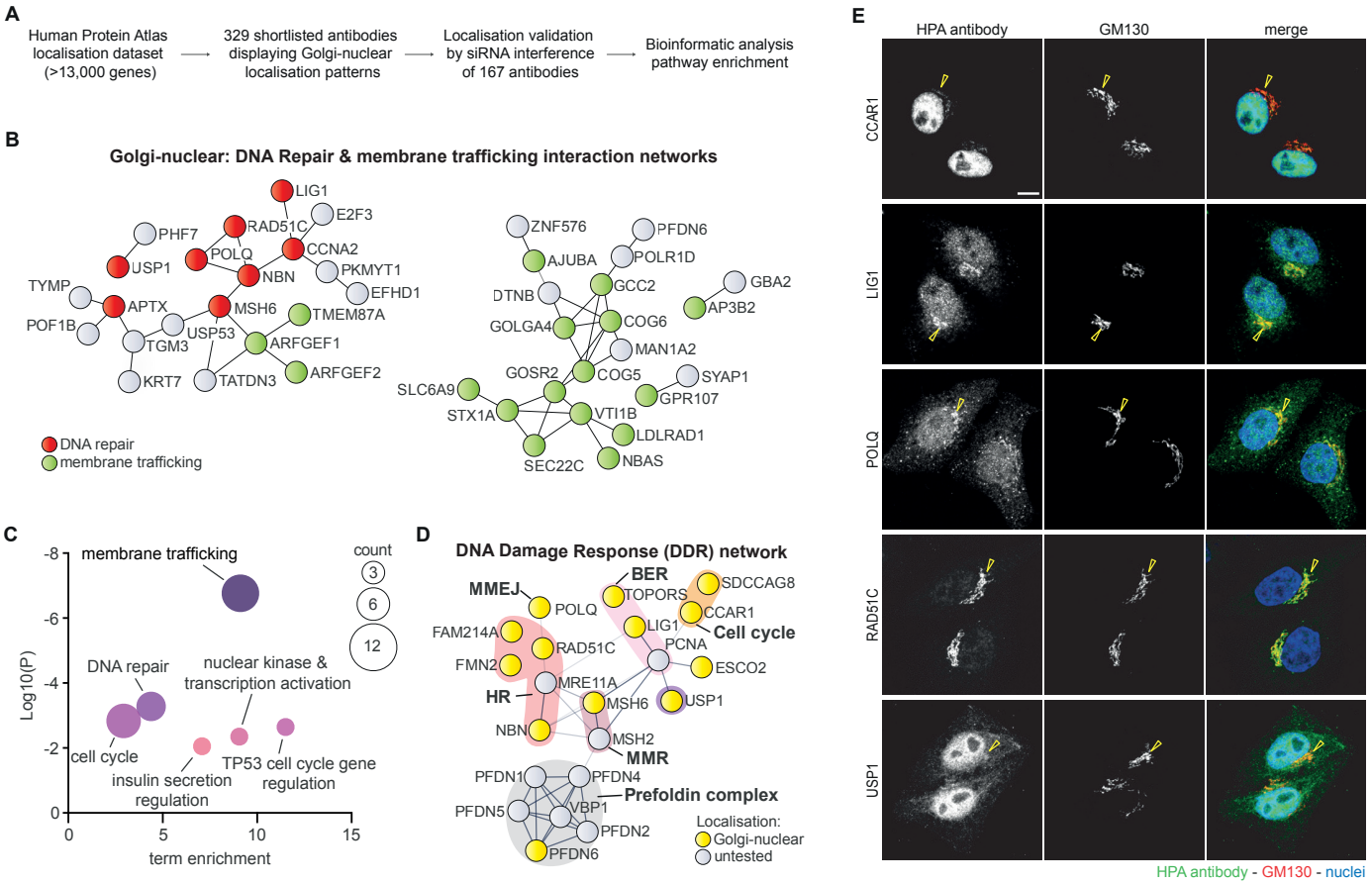

Figure 1: Antibody-based analysis identifies a network of DNA damage response (DDR) proteins at the Golgi complex
(A) Schematic diagram of the screening process for the shortlisting, validation and characterisation of Golgi-nuclear localisation proteins, as a strategy to identify linking pathways.
(B) Experimentally-based protein-protein interaction network displaying the DNA repair and membrane trafficking Golgi-nuclear localisation proteins validated in this study; categorised by functional pathways.
(C) Pathway enrichment analysis of the Golgi-nuclear localisation proteins identified in this study.
(D) Experimentally-based STRING protein-protein interaction network showing the DDR proteins identified to localise to both the Golgi complex and nucleus; yellow nodes indicate double-localising proteins, and grey nodes are filler untested proteins.
(E) Representative images of HeLa-K cells stained with Human Protein Atlas (HPA) antibodies against Golgi-nuclear DDR proteins (green), and the Golgi marker GM130 (red). DNA was stained with Hoechst 33342 (blue). Yellow arrowheads denote the Golgi complex. Scale bar, 10 µm.

Figure 2

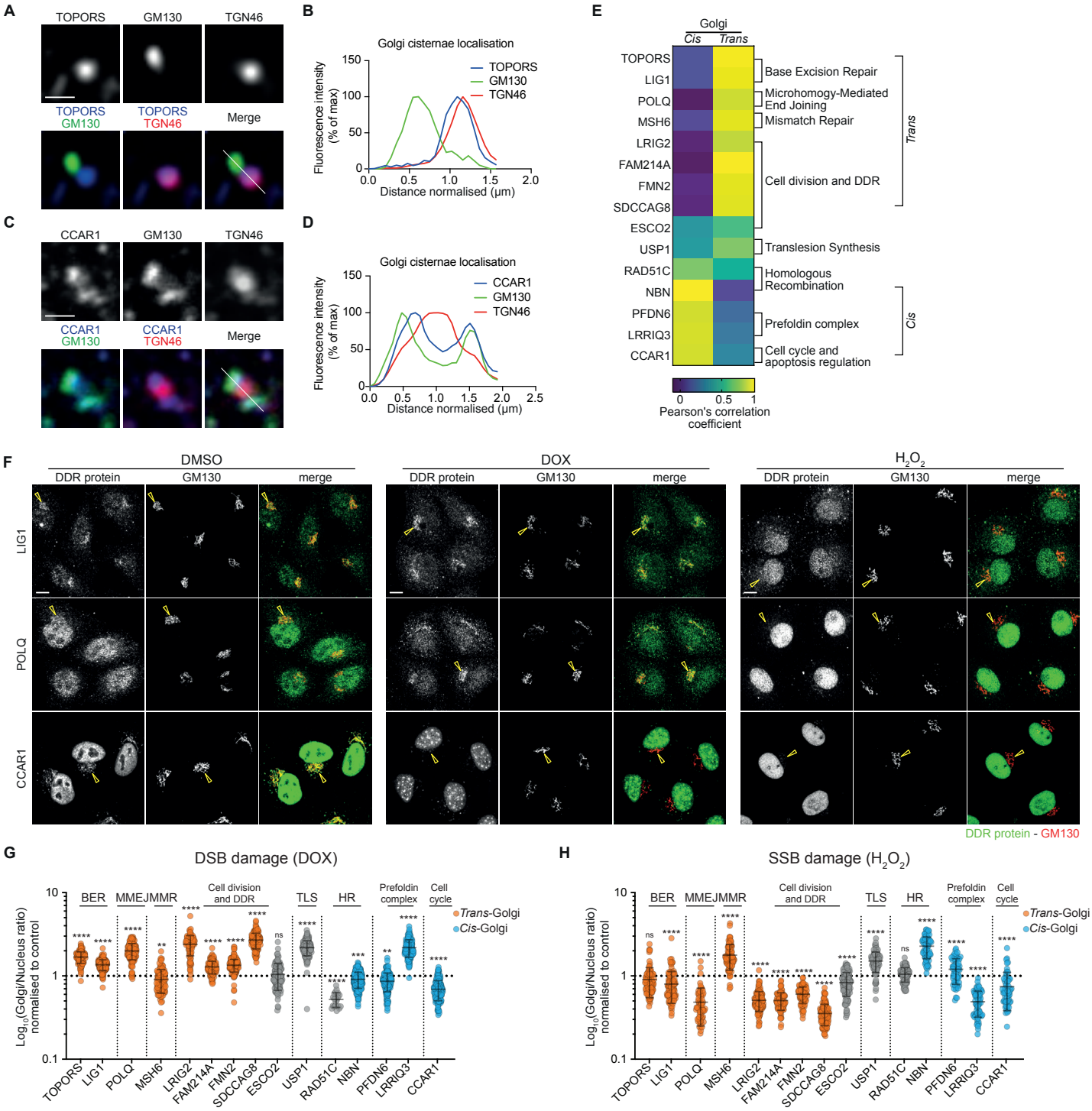

Figure 2: Systematic analysis of Golgi-nuclear DDR proteins localisation

(A–E) Golgi-cisternal localisation analysis of Golgi-nuclear DDR proteins. HeLa-K cells were treated with nocodazole (33 µM, 3 h), fixed and stained with antibodies against DDR proteins.

(A–C) Enlarged view of single isolated mini-stack, where cells were stained with antibodies against TOPORS, CCAR1 and Golgi markers GM130 (*cis*-Golgi) and TGN46 (*trans*-Golgi); scale bar, 1 µm; **(B-D)** white lines across the stack depict the line-plot analysis.

(E) Quantification of Pearson's correlation coefficient (PCC) between *cis*-Golgi and *trans*-Golgi markers and DDR proteins; n ≥ 36 mini-stacks.

(F) Localisation changes of dual-localising DDR proteins upon induction of DNA damage. HeLa-K cells were treated with the DNA damage-inducing drug, doxorubicin (DOX) (40 µM, 3 h) or oxidative stress-inducing agent hydrogen peroxide (H_2O_2) (50 µM for 20 min, followed with 15 min recovery), fixed and stained with antibodies against DDR proteins LIG1, POLQ, CCAR1 and the Golgi marker, GM130; yellow arrows denote the Golgi membranes. Scale bars, 10 µm.

(G) A ratio of DDR protein Golgi-nuclear distribution after treatment with DOX.

(H) A ratio of DDR protein Golgi-nuclear distribution after treatment with H_2O_2. Data represent the mean ± standard error of the mean (s.e.m.) (n = 3 biologically independent samples with at least 200 cells analysed for each protein in control and treatment conditions). The proteins are classified according to their Golgi localisation patterns **(E)**. Statistical significance was determined using a two-tailed unpaired Student's t-test; ns, **P < 0.01, ***P < 0.001, ****P <0.0001, compared to untreated control.

FIGURE 3

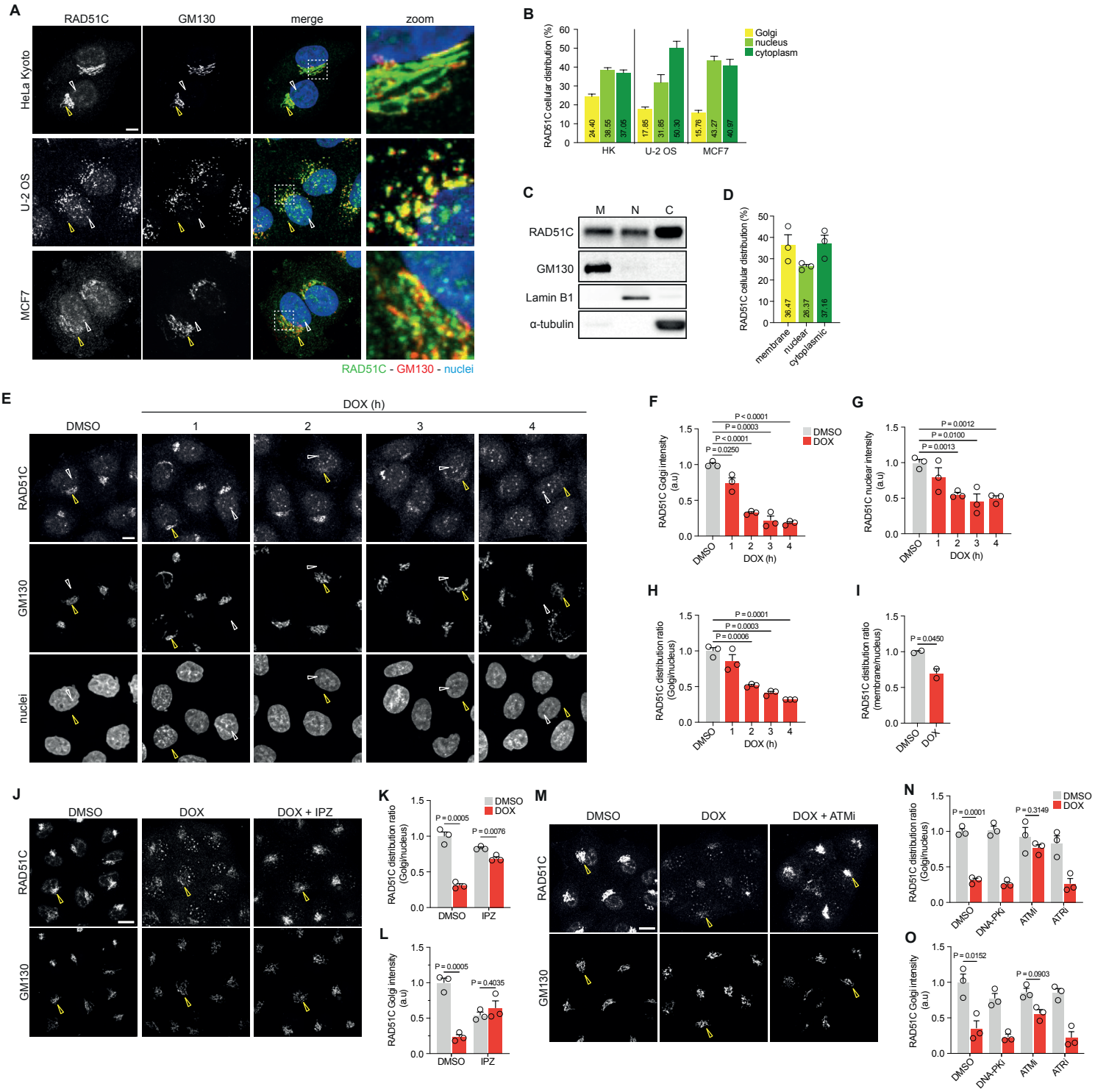

Figure 3: Redistribution of RAD51C Golgi fraction is required for the formation of RAD51C nuclear foci and is dependent on the kinase ATM

(A) Representative images of HeLa-K, U-2 OS and MCF7 cells stained with antibodies against RAD51C (green) and GM130 (red). DNA stained with Hoechst 33342 (blue). **(B)** Quantification of RAD51C distribution across the Golgi, nucleus and cytoplasm in various cell lines quantified from immunofluorescence images.

(C) WB analysis showing the subcellular membrane (M), nuclear (N) and cytoplasmic (C) fractions of RAD51C (markers: GM130 for Golgi membranes, Lamin B1 for the nuclear compartment, alpha-tubulin for the cytoplasmic fraction). **(D)** Quantification of western blot analysis showing the distribution of RAD51C in 3 cell fractions: membrane, nuclear and cytoplasmic; (n = 3 biologically independent experiments) data represent the mean ± s.e.m. **(E)** HeLa-K cells treated with the DNA damage-inducing drug, doxorubicin (DOX), for increasing lengths of time. Yellow arrows denote the Golgi membrane; white arrows denote nuclear foci. **(F)** Quantification of sum intensity of RAD51C Golgi population, **(G)** RAD51C nuclear population, and **(H)** a ratio of RAD51C Golgi-nuclear distribution after treatment with DOX. Data represent the s.e.m (n = 3 biologically independent samples with a total of 2343 cells analysed). **(I)** Quantification of RAD51C membrane-nuclear distribution ratio after treatment with DOX, calculated from isolated fractions **(Figure S6E)**. HeLa-K cells were stained with antibodies against RAD51C and GM130. **(J)** Cells were treated with DMSO or IPZ prior to a 3-hour treatment with DOX. Yellow arrows denote the Golgi membrane; white denote nuclear foci. Results were quantified as **(K)** ratio of RAD51C Golgi-nuclear distribution and **(L)** relative sum intensity of RAD51C at the Golgi Data represents s.e.m. (n = 3 biologically independent samples with a total of 445 cells analysed).

(M) HeLa-K cells were treated with DMSO (control) alone or with ATM inhibitor (KU55933) or ATR inhibitor (VE-821) or DNA-PK inhibitor (NU7441) prior to a 3-hour treatment with doxorubicin. Results were quantified as **(N)** ratio of RAD51C Golgi-nuclear distribution and **(O)** relative sum intensity of RAD51C at the Golgi. Data represents s.e.m. (n = 3 biologically independent samples with a total of 1679 cells analysed). Scale bars, 10 µm. Statistical significance was determined using a two-tailed unpaired Student's t-test.

FIGURE 4

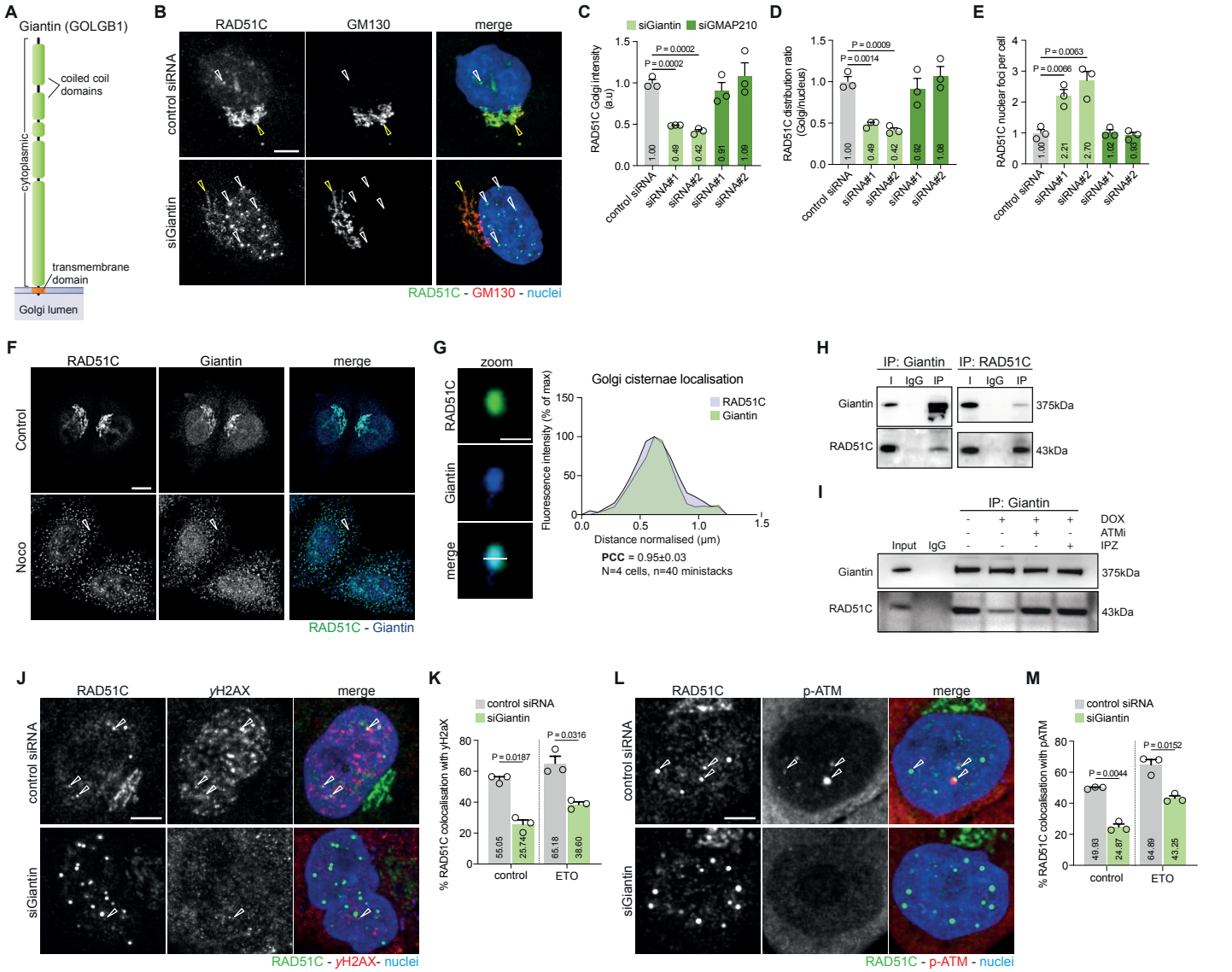

Figure 4: RAD51C Golgi localisation is dependent on the Golgin protein, Giantin

(A) Schematic diagram highlighting the domain organisation of Giantin.

(B) RAD51C protein redistribution upon depletion of Giantin. HeLa-K cells were transfected with either control or Giantin siRNAs for 72 h, then immunostained for RAD51C and the Golgi marker GM130. Yellow arrows mark the Golgi, and white arrows denote RAD51C nuclear foci.

(C–E) Quantifications of RAD51C localisation: **(C)** total Golgi-associated RAD51C intensity, **(D)** the Golgi-to-nucleus RAD51C intensity ratio, and **(E)** the number of nuclear RAD51C foci per cell. Data are presented as mean ± s.e.m. (n = 3 biologically independent experiments, 1,445 total cells).

(F) Golgi-cisternal co-localisation analysis. HeLa-K cells treated with Nocodazole (33 µM, 3 h), fixed and stained with antibodies against Giantin and RAD51C.

(G) Zoom enlarged view of single isolated mini-stack; scale bar, 1 µm; white line across the stack was used for line-scan analysis.

(H and I) Co-immunoprecipitation (co-IP) of endogenous Giantin with RAD51C under control conditions **(H)** or after doxorubicin (DOX) treatment and co-treatments with ATM inhibitor (ATMi) and importazole (IPZ) **(I)** in HeLa-K extracts.

(J–M) Co-localisation experiment of cells treated with control siRNA, or Giantin siRNA under control conditional or after treatment with ETO. Cells stained with antibodies against RAD51C (green) and HR DDR markers (red): **(J)** γ-H2AX, and **(L)** p-ATM. Co-localisation of structure is denoted by an arrowhead. Quantification of percentage RAD51C foci co-localising with **(K)** γ-H2AX and **(M)** p-ATM. Data represent the mean ± s.e.m. (n = 3 biologically independent samples with at least 200 cells and at least 550 RAD51C nuclear foci analysed for the co-localisation experiments for each condition).

FIGURE 5

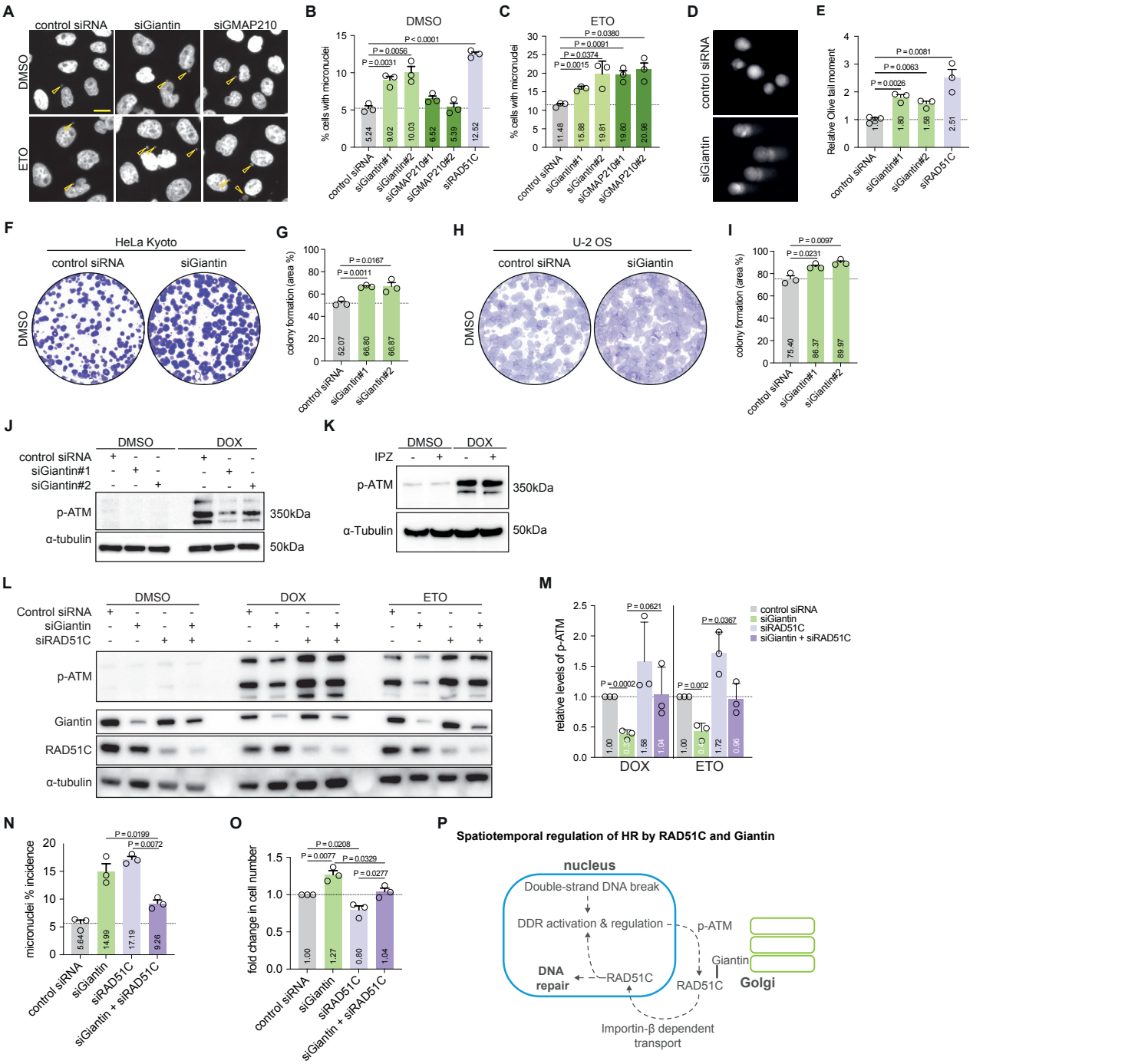

Figure 5: Spatial dysregulation of RAD51C by depletion of Giantin leads to genomic instability, inhibition of DDR signalling and accelerated cell proliferation

(**A–C**) Representative images and associated quantification of micronuclei formation following siRNA treatment under (**B**) basal condition and (**C**) after etoposide-induction DNA damage (10 μM; 16 h followed by 6 h recovery); yellow arrows denote micronuclei structures. Data represent the mean ± s.e.m. (n = 3 biologically independent samples with >10,000 cell analysed).

(**D**) Representative comet assay images measuring genomic DNA fragmentation in HeLa-K cells treated with control, Giantin, or RAD51C targeting siRNA.

(**E**) Quantification of OliveMoment from comet assay. Data represent the mean ± s.e.m. (n = 3 biologically independent samples).

(**F–I**) Representative colony formation assays in (**F**) HeLa-K and (**H**) U-2 OS cell lines with corresponding quantification of colony area coverage in (**G**) HeLa-K and (**H**) U-2 OS cells. Statistical significance was determined using a two-tailed unpaired Student's t-test. Scale bars, 10 μm.

(**J**) WB analysis of HeLa-K cells transfected with control and Giantin siRNA and treated with DOX (40 μM; 3 h). Extracts were prepared and immunoblotted as indicated (n = 2 biologically independent samples).

(**K**) WB of HeLa-K cells treated with DOX (40 μM; 3 h) and IPZ (20 μM; 3 h).

(**L**) WB of HeLa-K cells transfected with siRNAs against Giantin, RAD51C or a combination of both followed by treatment with DMSO, DOX (40 μM; 3h) or ETO (10 μM; 3 h) (**M**) with associated quantification showing the relative levels of pATM; (n=3 biological independent experiments), data represent the mean ± s.e.m.

(**N and O**) Quantification of micronuclei formation and fold change in cell number after siRNA treatments (mean ± s.e.m., n = 3, ≥1,000 cells per condition).

(**P**) Proposed model for the regulation of HR-mediated repair through the activation of RAD51C at the Golgi complex. RAD51C, a regulatory HR protein, is anchored to the Golgi through its interaction with the cytoplasmic tail of Giantin, in response to double-strand DNA breaks, this RAD51C Golgi population redistributes to form nuclear foci. This response requires Importin-beta-mediated nuclear import and the phosphorylation of ATM protein kinase. We propose that the Golgi functions as a spatiotemporal timing module that gates RAD51C (and other DDR factors) availability to ensure proper homologous recombination and DNA-damage signaling.

SUPPLEMENTARY FIGURE 1

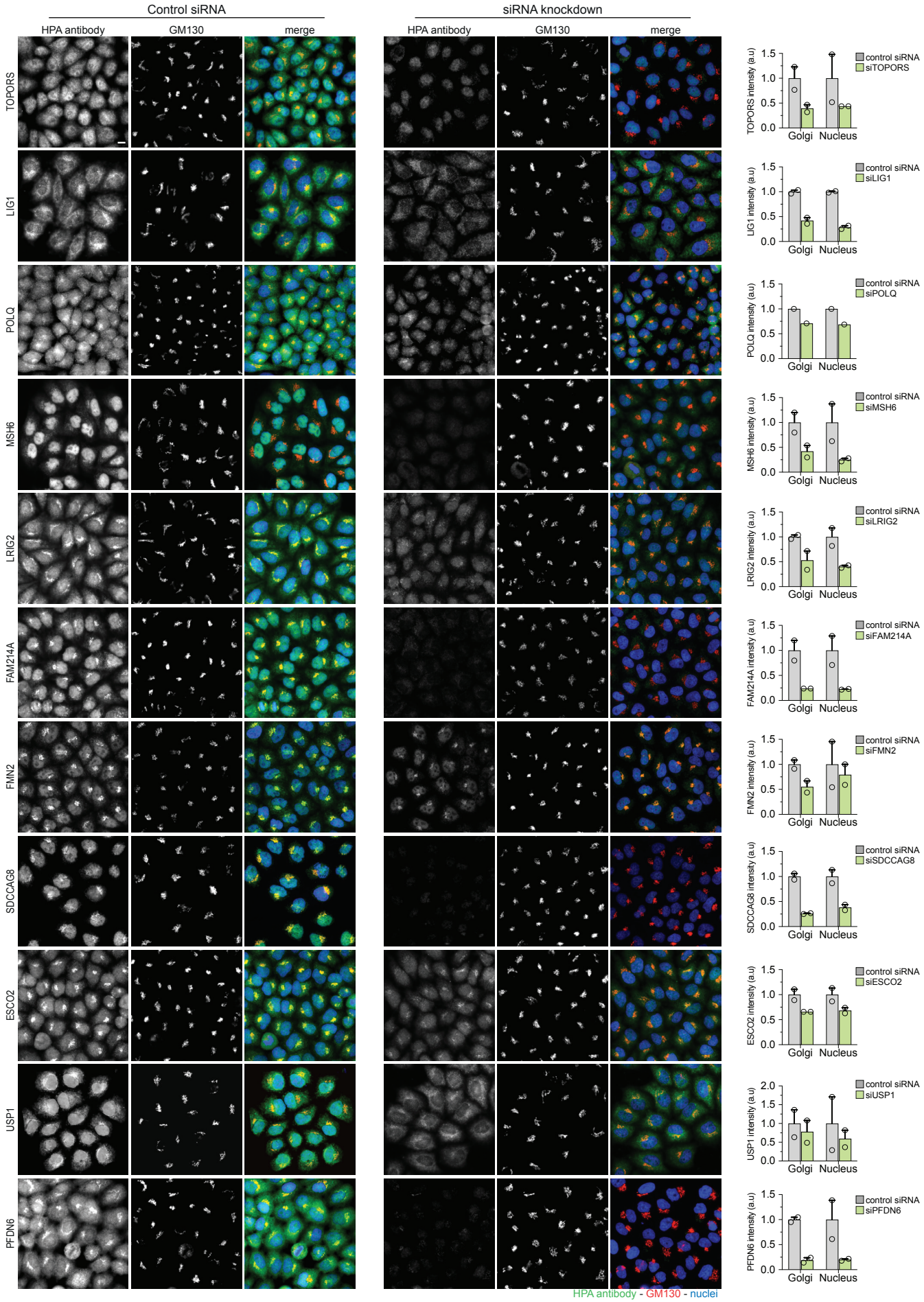

Figure S1: Validation of DDR protein antibody specificity and localisation, related fo Figure 1
Representative images of HeLa-K cells stained with antibodies against DDR proteins and the Golgi marker, GM130. Cells were treated with a control or an siRNA against the protein of interest to validate the specificity of the antibody. The changes in intensity measurements in the Golgi and nuclear compartment were quantified (n=2 for all proteins except for POLQ, which had n=1, biological independent samples with at least 500 cells analysed for each treatment). Scale bar, 10 µm. Continued on **Figure S2A**.

SUPPLEMENTARY FIGURE 2

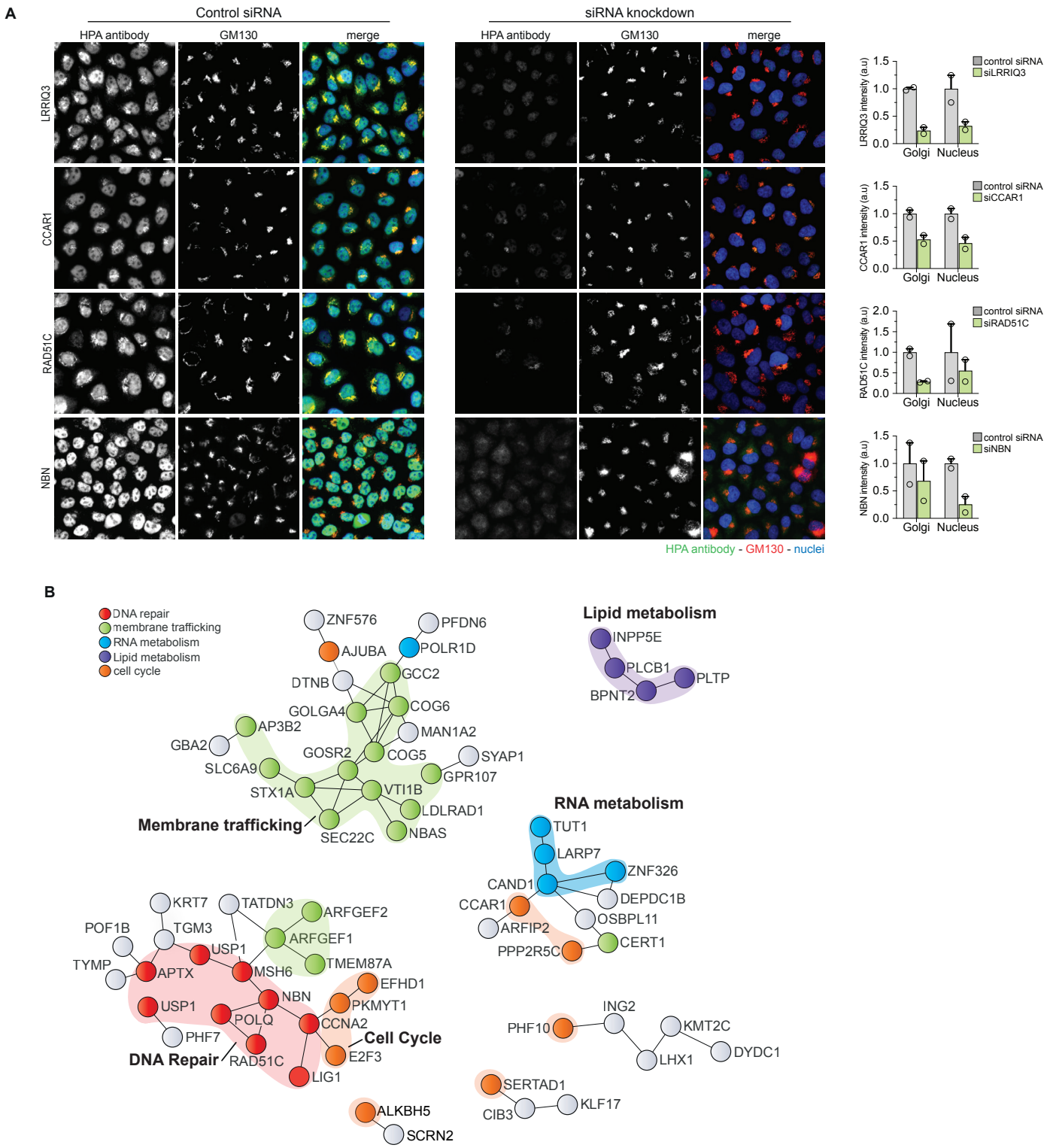

Figure S2: Validation of DDR protein localisation and functional network analysis, related to Figure 1
(A) Representative images of HeLa-K cells stained with antibodies against DDR proteins and the Golgi marker, GM130. Cells were treated with a control or an siRNA against the protein of interest to validate the specificity of the antibody. The changes in intensity measurements in the Golgi and nuclear compartment were quantified. (n=2, biological independent samples with at least 500 cells analysed for each treatment).
(B) Experimentally-based protein-protein interaction networks displaying the Golgi-nuclear localisation proteins validated in this study. Proteins are categorised by functional pathways annotated using gene ontology terms **(Table S1)**.

SUPPLEMENTARY FIGURE 3

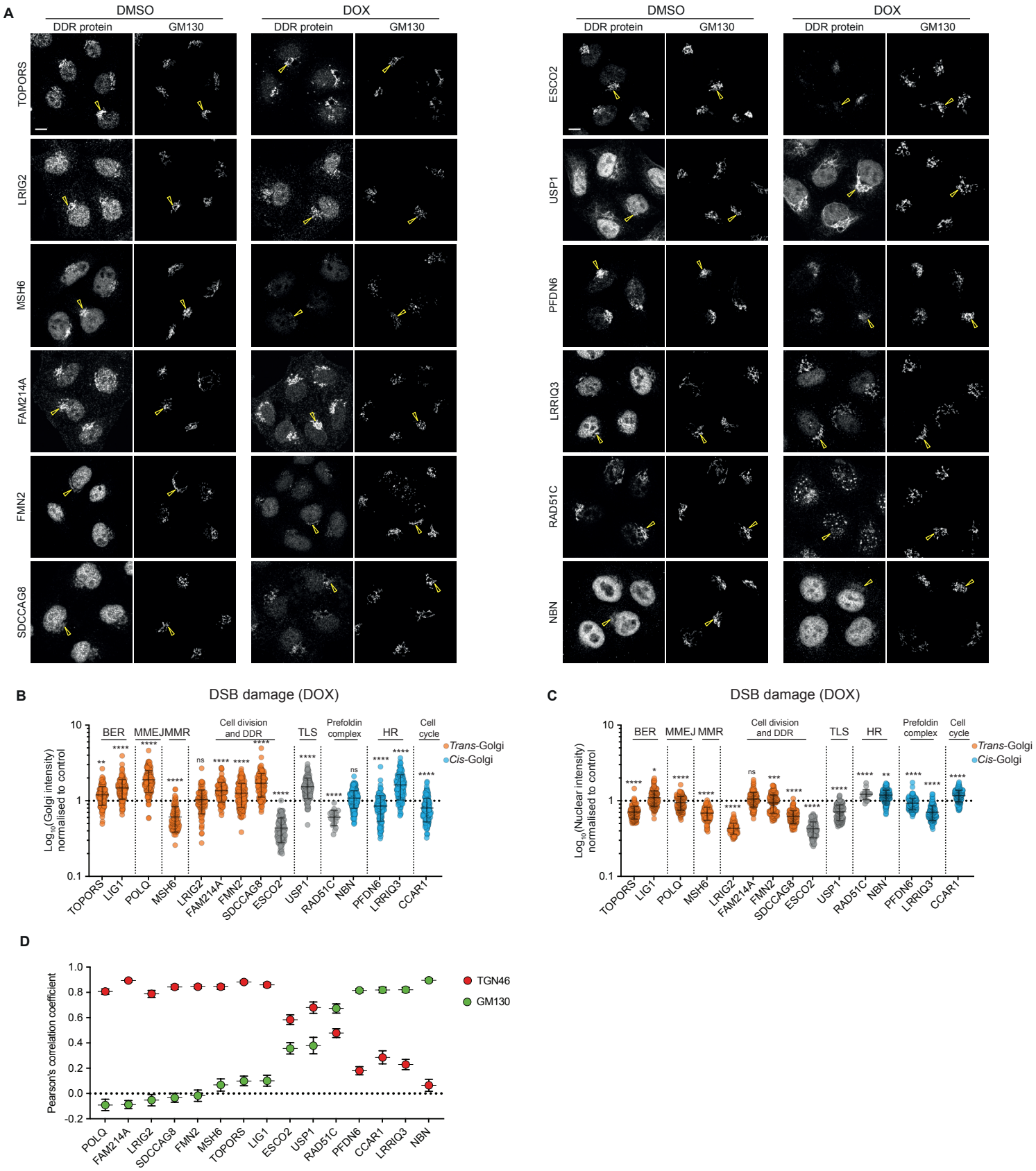

Figure S3: DOX-Induced Redistribution and Golgi-cisternal localisation analysis of DDR proteins, related to Figure 2
(A) Representative images of HeLa-K cells stained with antibodies against DDR proteins (green) and the Golgi marker, GM130 (red). Cells were treated with DOX (40 μM, 3 h), fixed, and immunostained. Yellow arrows denote Golgi membranes. Scale bars, 10 μm.
(B and C) Quantification of DDR protein intensity changes upon DOX treatment. **(B)** Relative intensity of DDR proteins at the Golgi and **(C)** in the nucleus, normalised to untreated control. Data represent the mean ± s.e.m. (n = 3 biologically independent samples with at least 200 cells analysed for each protein in control and treatment conditions). The proteins are classified according to their Golgi localisation patterns **(Figure 2E)**. Statistical significance was determined using a two-tailed unpaired Student's t-test; ns P > 0.05, *P < 0.05, **P < 0.01, ***P < 0.001, ****P <0.0001, compared to untreated control.
(D) Golgi-cisternal localisation analysis of Golgi-nuclear DDR proteins. HeLa-K cells were treated with Nocodazole (33 μM, 3 h), fixed and stained with antibodies against DDR proteins. Quantification of Pearson's correlation coefficient (PCC) between cis-Golgi and trans-Golgi markers and DDR proteins; N ≥ 4 cells; n ≥ 36 mini stacks.

SUPPLEMENTARY FIGURE 4

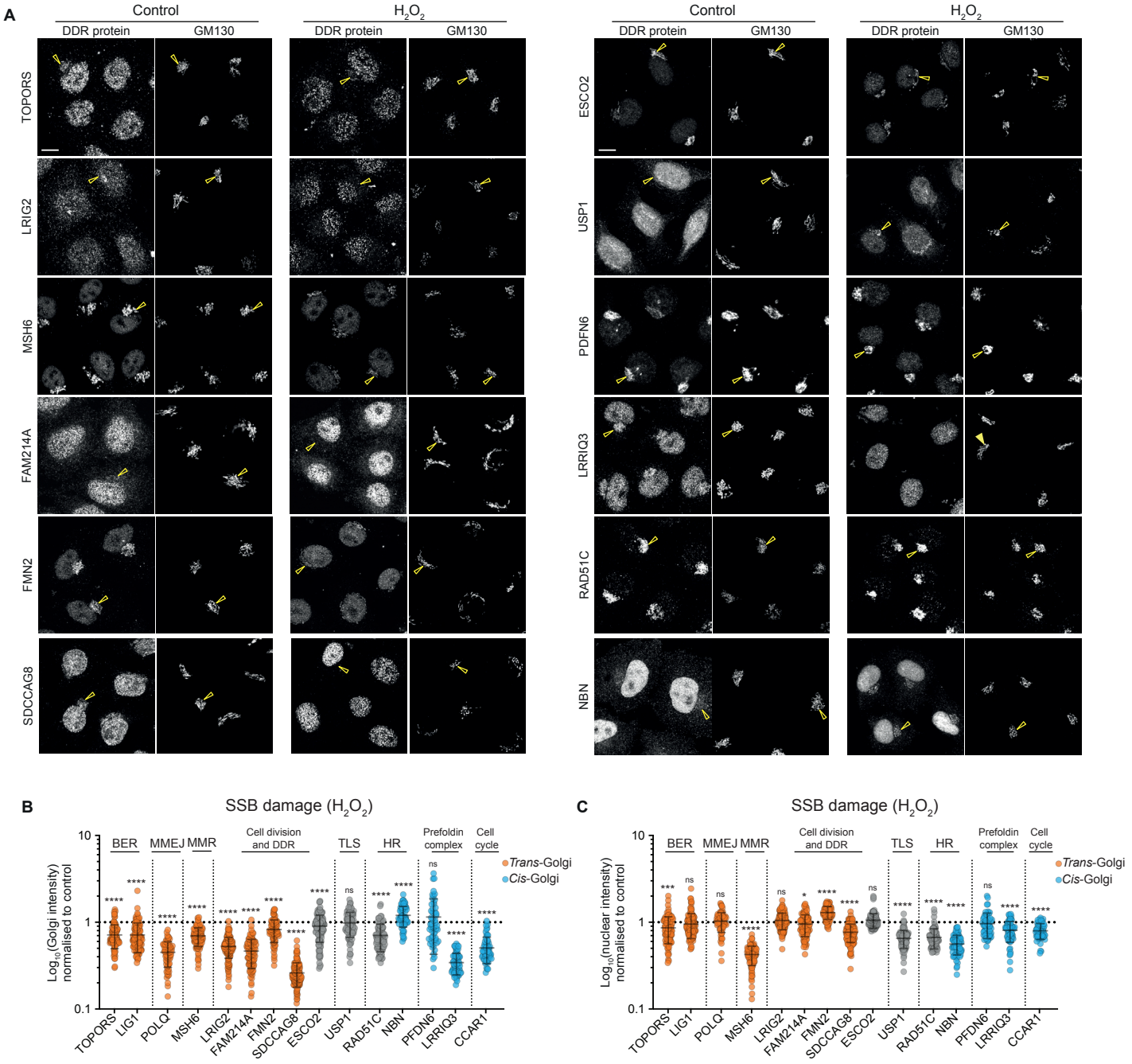

Figure S4: H_2O_2-Induced redistribution of DDR proteins, related to Figure 2
(A) Representative images of HeLa-K cells were stained with antibodies against DDR proteins and the Golgi marker, GM130. HeLa-K cells were treated with H2O2 (50 µM, for 20 min followed by 15 min recovery), fixed and stained with antibodies against DDR proteins and the Golgi marker, GM130; yellow arrows denote the Golgi membranes. Scale bars, 10 µm.
(B and C) Quantification of DDR protein intensity changes upon H_2O_2 treatment. **(B)** Relative intensity of DDR proteins at the Golgi and **(C)** in the nucleus, normalised to untreated control. Data represent the mean ± s.e.m. (n = 3 biologically independent samples with at least 200 cells analysed for each protein in control and treatment conditions). The proteins are classified according to their Golgi localisation patterns **(Figure 2E).** Statistical significance was determined using a two-tailed unpaired Student's t-test; ns P > 0.05, *P < 0.05, ***P < 0.001, ****P <0.0001, compared to untreated control.

SUPPLEMENTARY FIGURE 5

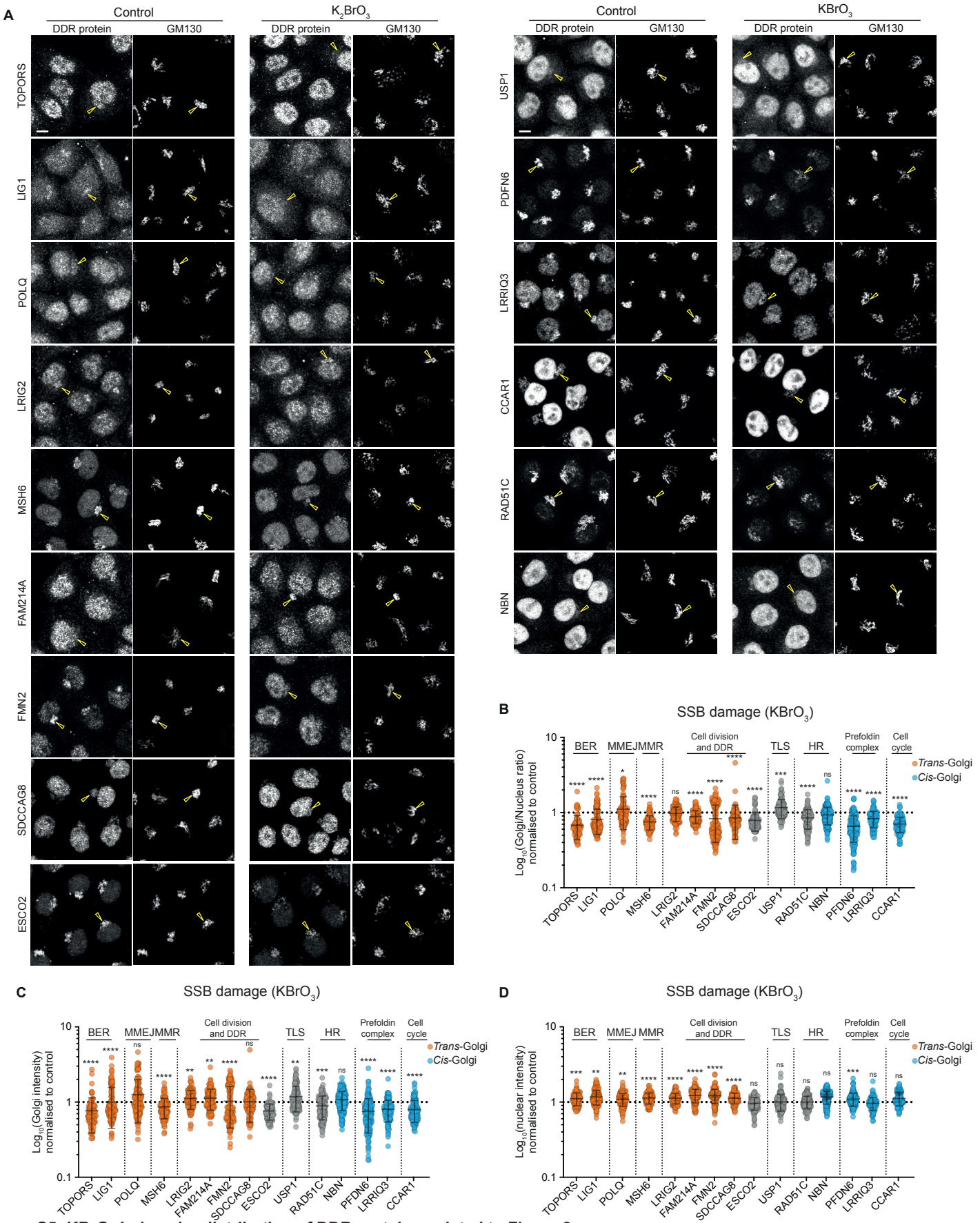

Figure S5: $KBrO_3$-Induced redistribution of DDR proteins, related to Figure 2

(A) Representative images of HeLa-K cells were stained with antibodies against DDR proteins and the Golgi marker, GM130. HeLa-K cells were treated with $KBrO_3$ (5 mM, 3h), fixed and stained with antibodies against DDR proteins and the Golgi marker, GM130 (A to D); yellow arrows denote the Golgi membranes. Scale bar, 10 µm.

(B) A ratio of DDR protein Golgi-nuclear distribution after treatment with $KBrO_3$.

(C and D) Quantification of DDR protein intensity changes upon $KBrO_3$ treatment. **(C)** Relative intensity of DDR proteins at the Golgi and **(D)** in the nucleus, normalised to untreated control. Data represent the mean ± s.e.m. (n = 3 biologically independent samples with at least 200 cells analysed for each protein in control and treatment conditions). The proteins are classified according to their Golgi localisation patterns **(Figure 2E)**. Statistical significance was determined using a two-tailed unpaired Student's t-test; ns P > 0.05, *P < 0.05, **P < 0.01, ***P < 0.001, ****P <0.0001, compared to untreated control.

SUPPLEMENTARY FIGURE 6

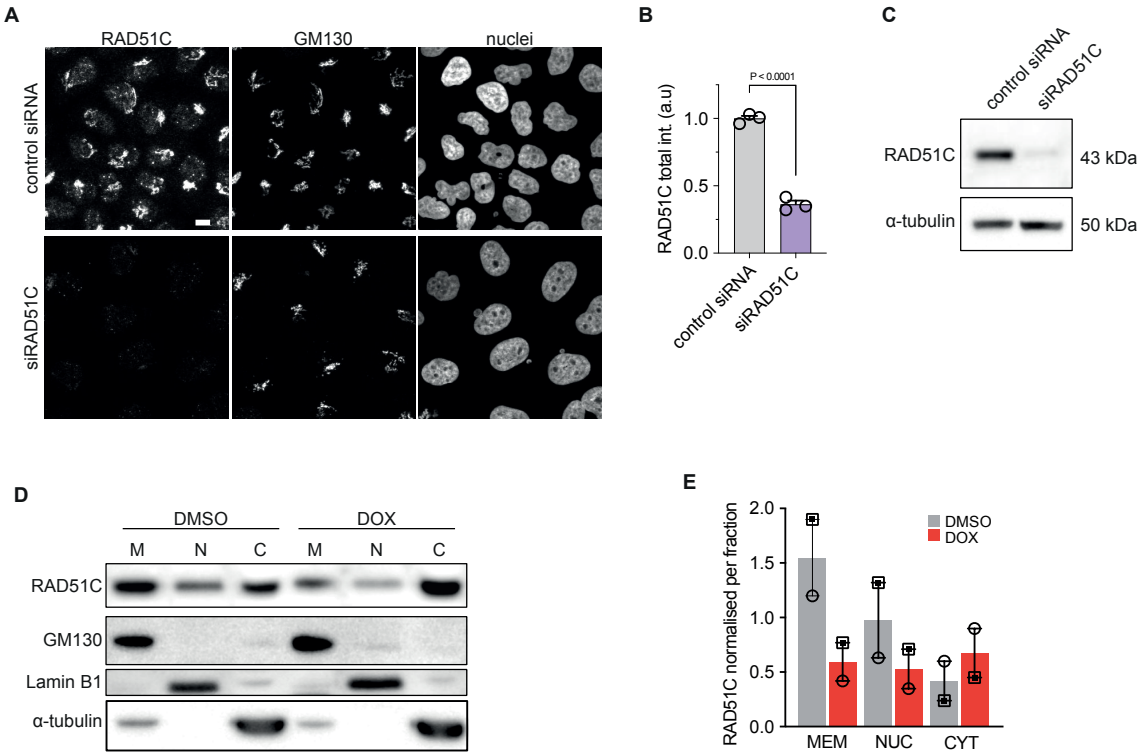

Figure S6: Validation of RAD51C subcellular localisation, related to Figure 3

(A) Representative images showing the RAD51C antibody specificity. HeLa-K cells were stained with antibodies against RAD51C and GM130; DNA was stained with Hoechst 33342. Scale bar, 10 µm.

(B) Quantification of RAD51C sum intensity after RAD51C depletion. Data represent the mean ± s.e.m. (n = 3 biologically independent samples with a total of 831 cells analysed).

(C) Western blot analysis showing the level of RAD51C protein level, in RAD51C-depleted and control cells (n = 3 biologically independent samples). Statistical significance was determined using a two-tailed unpaired Student's t-test.

(D) Western blot analysis showing the subcellular localisation of RAD51C treated with the DMSO and doxorubicin. The protein levels normalised against the respective fraction control (RAD51Cmem/GM130; RAD51Cnuc/Lamin B1; RAD51Ccyt/tubulin). Data represent the mean ± s.e.m; (n = 2 biologically independent samples).

(E) Quantification of RAD51C membrane-nuclear distribution ratio after treatment with DOX, calculated from isolated fractions.

SUPPLEMENTARY FIGURE 7

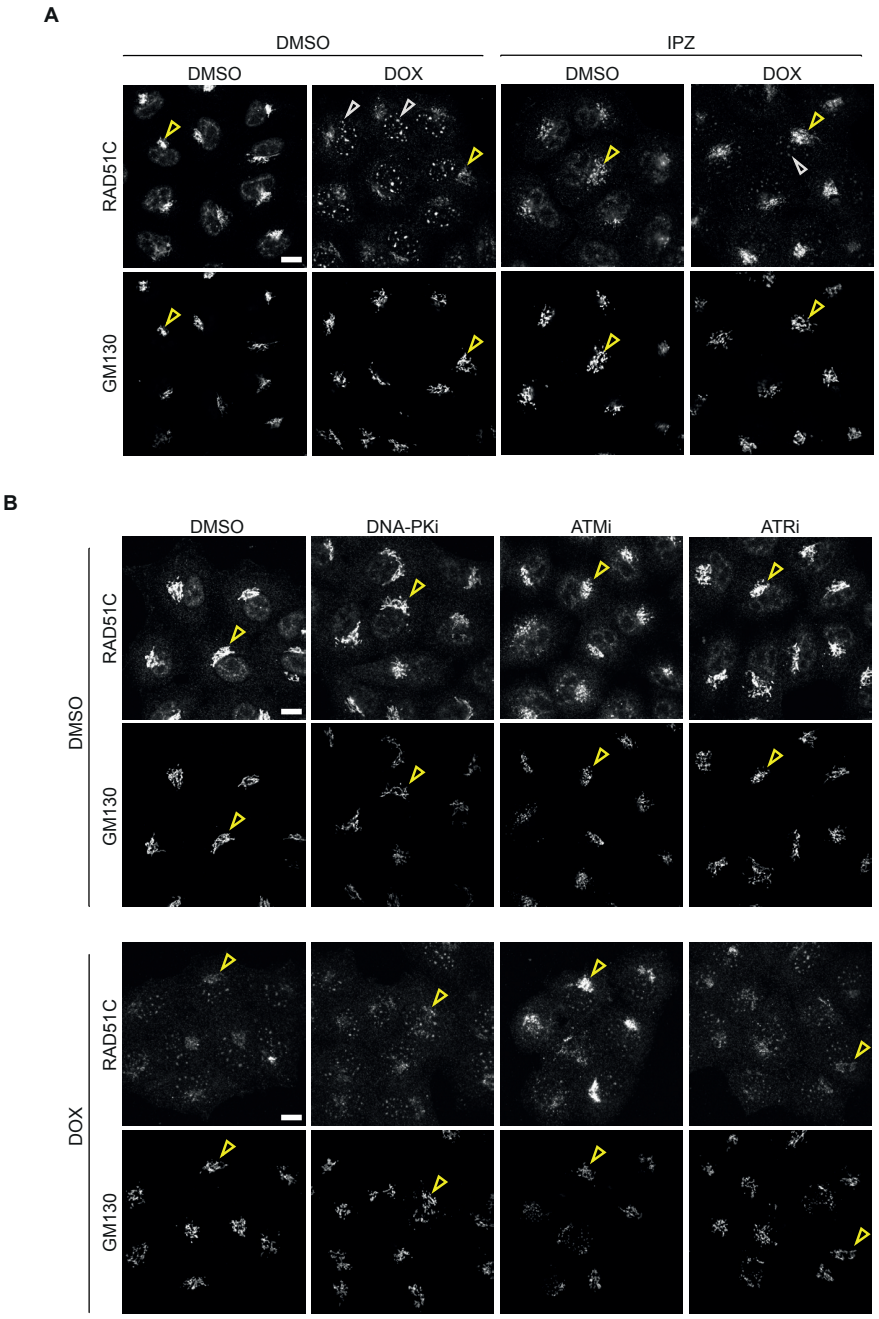

Figure S7: RAD51C Golgi population redistribution upon treatment with IPZ and inhibition of DDR signalling, related to Figure 3
(A) Representative images of the RAD51C protein redistribution upon treatment with IPZ and DOX. HeLa-K cells were stained with antibodies against RAD51C and GM130. Cells were treated with DMSO or IPZ prior to a 3-hour treatment with DOX.
(B) Representative images of the RAD51C protein redistribution upon treatment with DDR signalling inhibitors and DOX. HeLa-K cells were treated with DMSO (control) alone or with ATM inhibitor (KU55933), ATR inhibitor (VE-821) or DNA-PK inhibitor (NU7441) prior to a 3-hour treatment with doxorubicin. Yellow arrows denote the Golgi membrane; white denotes nuclear foci. Scale bars, 10 µm.

SUPPLEMENTARY FIGURE 8

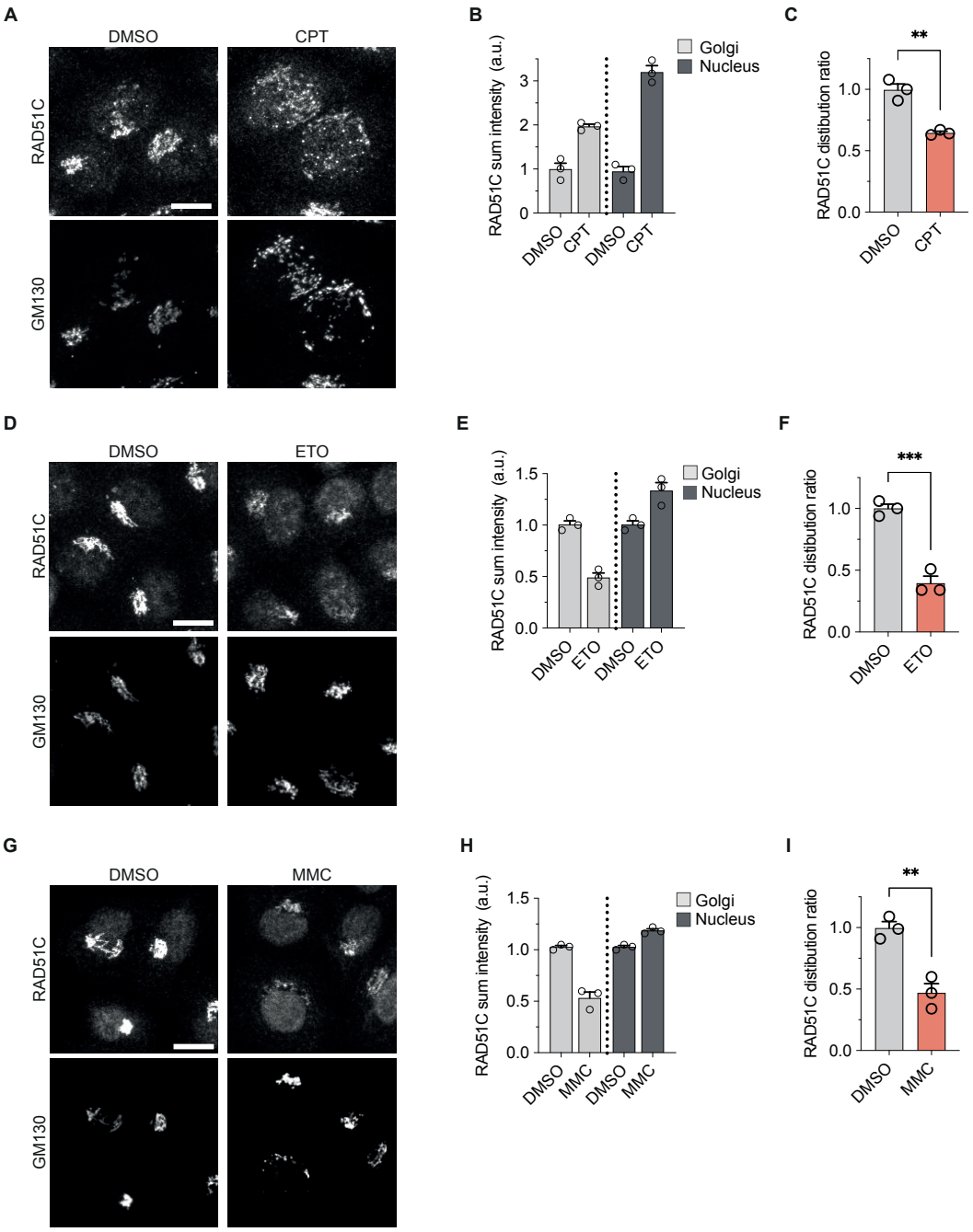

Figure S8: RAD51C protein localisation and redistribution upon induction treatment with DNA damage agents, related to Figure 3
(A) Representative images of HeLa-K cells stained with antibodies against RAD51C and GM130 after treatment with Camptothecin (CPT) for 16 h followed by media change for 2 h. Scale bar, 10 µm.
(B) Quantification of RAD51C distribution between the Golgi and nuclear compartments after CPT treatment.
(C) Quantification of RAD51C distribution ratio between the Golgi and nuclear compartments after CPT treatment.
(D) Representative images of HeLa-K cells stained with antibodies against RAD51C and GM130 after treatment with Etoposide (ETO) for 16 hours followed by media change for 2 h. Scale bar, 10 µm.
(E) Quantification of RAD51C distribution between the Golgi and nuclear compartments after ETO treatment.
(F) Quantification of RAD51C distribution ratio between the Golgi and nuclear compartments after ETO treatment.
(G) Representative images of HeLa-K cells stained with antibodies against RAD51C and GM130 after treatment with Mitomycin C (MMC)for 16 h followed by media change for 2 h. Scale bar, 10 µm.
(H) Quantification of RAD51C distribution between the Golgi and nuclear compartments after MMC treatment.
(I) Quantification of RAD51C distribution ratio between the Golgi and nuclear compartments after ETO treatment.
Data represent the mean ± s.e.m. (n = 3 biologically independent samples with more than 600 cells analyzed per treatment). Statistical significance was determined using a two-tailed unpaired Student's t-test. **P < 0.01; ***P < 0.001.

SUPPLEMENTARY FIGURE 9

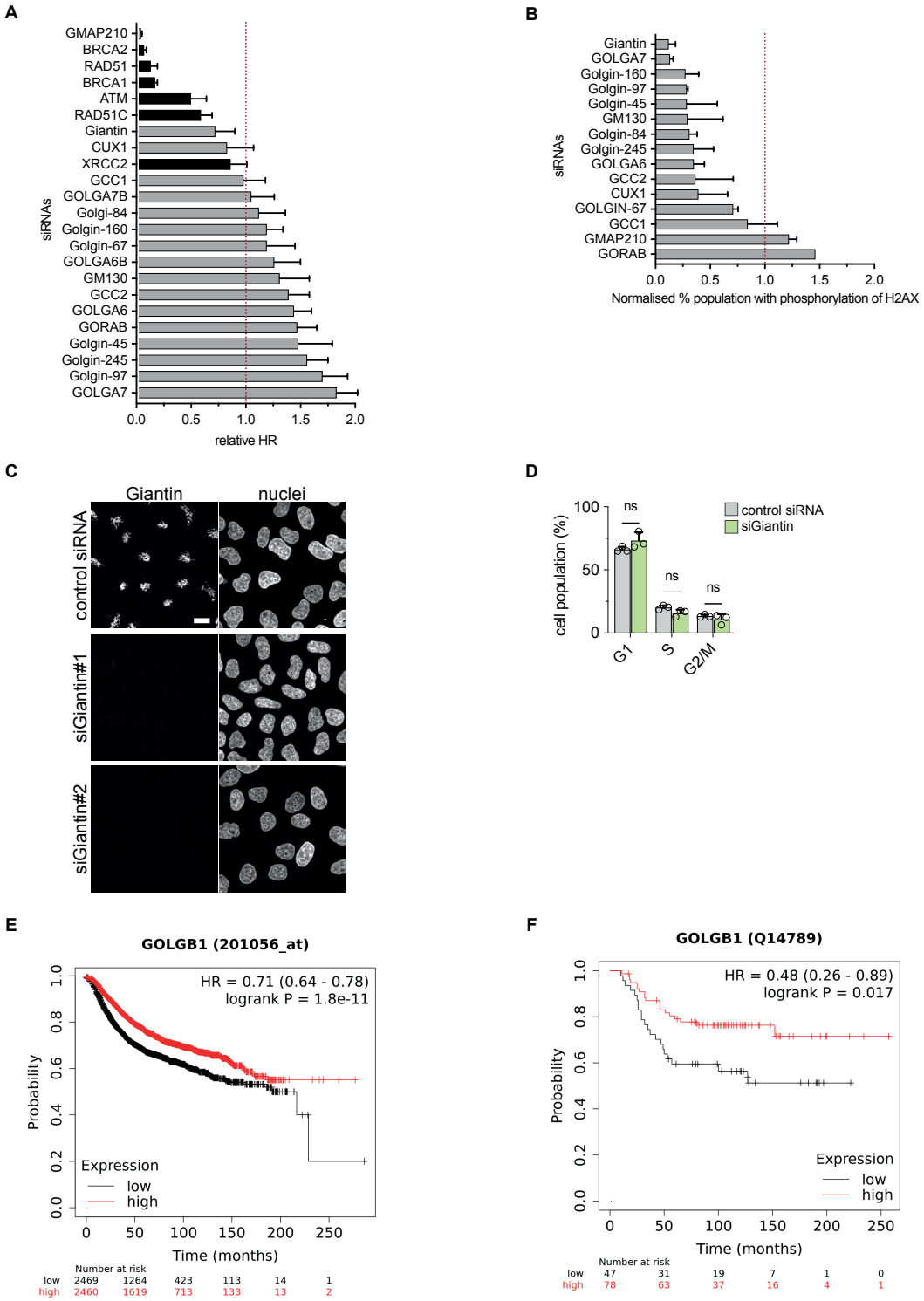

Figure S9: Impact of Golgin proteins on DNA repair, cell cycle, and breast cancer survival, related to Figure 4 and Figure 5
(A) Re-analysed siRNA screen data (Adamson et al., 2012) showing the relative Homologous Recombination (HR) repair rate upon systematic knockdown of the Golgin protein family (grey) and HR complex proteins (black).
(B) Re-analysed siRNA screen data (Paulsen et al., 2009) showing the relative percent cell population with phosphorylation of H2AX upon systematic knockdown of the Golgins. The datasets are normalised to the negative control set at 1.
(C) HeLa-K cells were transfected with control, or Giantin siRNAs for 72 hours. The cells were stained with antibodies against Giantin and nuclei were stained with Hoechst 33342. Scale bar, 10 µm.
(D) Cell cycle profile of HeLa-K cell treated with Giantin or control siRNA. Data represent the mean ± s.e.m. (n = 3 biologically independent samples).
(E and F) Kaplan-Meier survival plots in patients with high and low mRNA **(F)** (Győrffy, 2021) and protein **(G)** (Ősz et al., 2021) Giantin expression in Breast Cancer patients. The graph was generated using the kmplot database (https://kmplot.com).